Petroleum Science 23 (2026) 5400–5417

Contents lists available at ScienceDirect

Petroleum Science

journal homepage: www.keaipublishing.com/en/journals/petroleum-science

Original Paper

A rock physics modeling for hydrate–gas and gas–water mixing in marine sediments

Jin Qian [a,b,*], Xiu-Juan Wang [c,b], Zhen Liu [a], Qiao-Qiao Wang [a], Jia-Peng Jin [d,**], Neng-You Wu [d]

[a] School of Resources and Geosciences, China University of Mining and Technology, Xuzhou, 221116, Jiangsu, China
[b] Laboratory for Marine Mineral Resources, Qingdao Marine Science and Technology Center, Qingdao, 266237, Shandong, China
[c] Frontiers Science Center for Deep Ocean Multispheres and Earth System, Key Laboratory of Submarine Geosciences and Prospecting Techniques, MOE and College of Marine Geosciences, Ocean University of China, Qingdao, 266100, Shandong, China
[d] Laoshan Laboratory, Qingdao, 266100, Shandong, China

ARTICLE INFO

Article history:
Received 7 November 2025
Received in revised form
21 January 2026
Accepted 30 March 2026
Available online 2 April 2026

Edited by Meng-Jiao Zhou

Keywords:
Gas hydrate
Free gas
Coexisting
Rock physics model
Multiphase mixing

ABSTRACT

In 2017 and 2020, China successfully performed two hydrate production tests near Sites GMGS3-W17 and GMGS6-SH2 in the northern South China Sea. Two tests revealed that large amounts of free gas are enriched below the bottom simulating reflection (BSR). However, hydrate saturations at this depth derived from chlorinity data and a pressure core range from 27% to 41%. Well log data in this interval are characterized by low P-wave velocity and high resistivity. Therefore, resistivity-derived hydrate saturations are much higher than P-wave velocity-derived values. This discrepancy occurs because free gas would induce a sharp decrease in P-wave velocity. Currently, the gas–water mixing model is commonly employed to resolve this discrepancy. To improve accuracy, we develop a novel rock physics model of multiphase mixing coexistence including solid phase, hydrate–gas phase, and gas–water phase. The model is applicable to both isotropic and anisotropic hydrate reservoirs. To validate its accuracy, the model and well log data are utilized to predict saturations at six sites worldwide where hydrates and free gas coexist. The predicted hydrate and gas saturations are consistent with those derived from pressure cores and chlorinity data. This suggests that the model can be robustly used for quantitative characterization of hydrate when coexisting with free gas. Therefore, our model will provide an accurate method for the resource predictions of hydrate and free gas in such coexisting sediments, especially those below the conventional BSR. It will also facilitate the understanding of the fluid distributions in such a complex three-phase coexistence system in nature.

1. Introduction

In nature, three different structures of hydrates, namely structures I, II (sI, sII, Kvenvolden, 1993) and H (sH, Lu et al., 2007), have been identified. These structures are composed of different hydrocarbon gases, inducing the complexity of the hydrate systems (Sloan and Koh, 2008). In the marine environments, the bottom simulating reflection (BSR/sI-BSR) corresponds approximately to the base of sI methane hydrate stability zone (sI-BHSZ) (Singh et al., 1993). The sII-BHSZ is occasionally accompanied by the sII-BSR (Tréhu et al., 2003), and is deeper due to the heavier hydrocarbons (Lu et al., 2007). The deep sII hydrates will not only increase the current predicted hydrate resources, but also provide a buffer for hydrocarbon expulsion (Klapp et al., 2010). Furthermore, hydrates can coexist with free gas in such a complex system (Tréhu et al., 2003).

There have been multiple reports worldwide regarding the coexistence of hydrate and free gas (Fig. 1). At Site 892 along Central Oregon Margin, the theoretical depth of I-BHSZ is deeper than the depth of I-BSR (Whiticar et al., 1995). Well logs indicate that free gas is present between I-BHSZ and I-BSR (Westbrook et al., 1994). In the Blake Ridge, the measured bulk modulus at Site 995 (Guerin et al., 1999) indicates that hydrates even occur below the I-BSR, and thus coexist with free gas. The coexistence can also be observed above the I-BSR at Sites 1249 (Milkov et al., 2004) and

* Corresponding author.
** Corresponding author.
E-mail addresses: qianjin@cumt.edu.cn (J. Qian), jpjin@lsnl.cn (J.-P. Jin).
Peer review under the responsibility of China University of Petroleum (Beijing).

https://doi.org/10.1016/j.petsci.2026.03.064

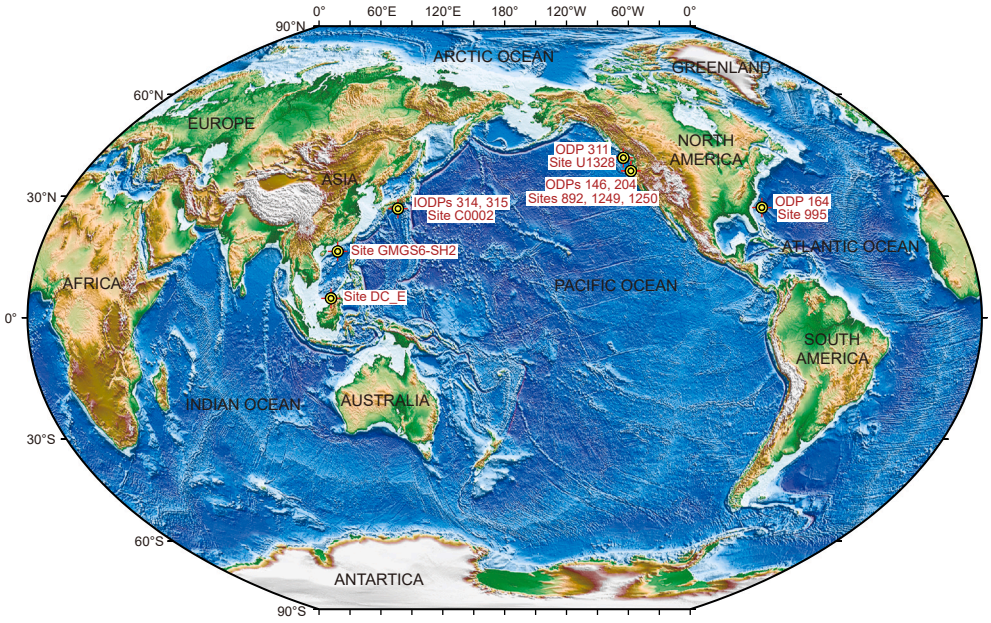

Fig. 1. Location map showing reported coexistence of hydrate and free gas (yellow circles).

C0002 (Miyakawa et al., 2014) in the Hydrate Ridge and the Nankai Trough, respectively. Geochemical analyses have also revealed the coexistence of sI and sII hydrates above the I-BHSZ in Lake Baikal (Kida et al., 2006), the Gulf of Mexico (Klapp et al., 2010) and the South China Sea (Wei et al., 2018). This demonstrates that biogenic and thermogenic gases can form hydrates simultaneously. At Site U1328, the presence of sII hydrates and the associated free gas at and below the BSR is revealed from the elevated concentrations of higher order hydrocarbons in the cores (Expedition 311 Scientists et al., 2006a). This coexistence has been further confirmed from the cores (Paganoni et al., 2016) and two hydrate production tests (Li et al., 2018; Ye et al., 2020) in the South China Sea.

Low P-wave velocity, slightly high S-wave velocity, and high resistivity (Guerin et al., 1999; Paganoni et al., 2016) are significant characteristics of the sediments where hydrates coexist with free gas. They are similar to those of gas-bearing sediments, but occasionally exhibit relatively high P-wave velocity (Qian et al., 2018). The saturations calculated from velocity well logs are inconsistent with those from resistivity well logs (Lee and Collett, 2006). This discrepancy affects the accurate calculation of hydrate and free gas resources. At Site 995, hydrate saturations below the I-BSR were calculated using the cementation theory and the fluid Reuss average at a constant gas saturation of 1% (Guerin et al., 1999). The calculated hydrate saturations are close to that derived from a pressure core. At Sites 1244, 1245, and 1247, hydrate and gas saturations were derived from S- and P-wave velocity logs, respectively. The saturations demonstrate that hydrates coexist with free gas within the HSZ (Lee and Collett, 2006). Above the BSR at Site C0002, hydrate saturations derived from resistivity log are generally higher than those derived from P-wave velocity logs (Miyakawa et al., 2014). In the presence of free gas, P-wave velocity-calculated saturations are underestimated, whereas resistivity-calculated saturations represent the sum of gas and hydrate. To understand the elastic wave attenuation mechanism of fluid inclusions in pore-filling hydrate, Marín-Moreno et al. (2017) developed a hydrate-bearing effective model. The simplified three phase equation (STPE) (Qian et al., 2018) and this effective model (Qin et al., 2020) were respectively applied to predict hydrate and gas saturations at Sites GMGS3-W17 and GMGS6-SH2, offshore China. Most of the above calculations directly use Reuss average of gas and water (Lee and Collett, 2006; He et al., 2025) to model the coexistence of gas and hydrate. However, the hydrate samples in the Cascadia margin have a globular fabric with cavities created by gas bubbles, and hydrates precipitate only on the surface of the cavities, namely the gas-water interface (Bohrmann et al., 1998). Similar structures of a hydrate film enveloping gas have recently been discovered in laboratory experiments (Sahoo et al., 2018).

The previous discrepancy between hydrate saturations derived from velocity and resistivity logs could be attributed to the factors such as clay/fracture-induced anisotropy, hydrates heterogeneity, and specific geological conditions (Pecher et al., 2003; Kumar et al., 2006; Lee and Collett, 2011; Jana et al., 2015). In this paper, the coexistence of hydrate and free gas can also lead to such a discrepancy. Therefore, to overcome this discrepancy, a new model is required to solve the direct contact between hydrate and gas. Here, we present a novel rock physics model for multiphase mixing in marine hydrate and free gas-coexisting sediments. The effective medium theory (EMT) is employed to develop a direct contact phase between hydrate and gas. The model assumes that the sediments consist of three components including solid phase, hydrate–gas phase, and gas–water phase (Fig. 2). The model is validated using well logs from several regions around the world that contain coexistence interval of hydrate and gas. The calculated saturations are consistent with those derived from chlorinity data and pressure cores. Our model will provide an accurate method for the resource predictions of hydrate and free gas in such coexisting sediments, especially those below the conventional BSR.

2. Coexistence model of hydrate–gas–water (CMHGW)

Core and resistivity imaging data show that both fracture-filling (Paganoni et al., 2016) and pore-filling hydrates (Yang et al., 2017) can coexist with free gas in nature, possibly dominated by a hydrate film enveloping gas (Bohrmann et al., 1998; Sahoo et al., 2018). Hydrate-bearing sediments with fracture- and pore-filling exhibit significantly different elastic (Lee and Collett,

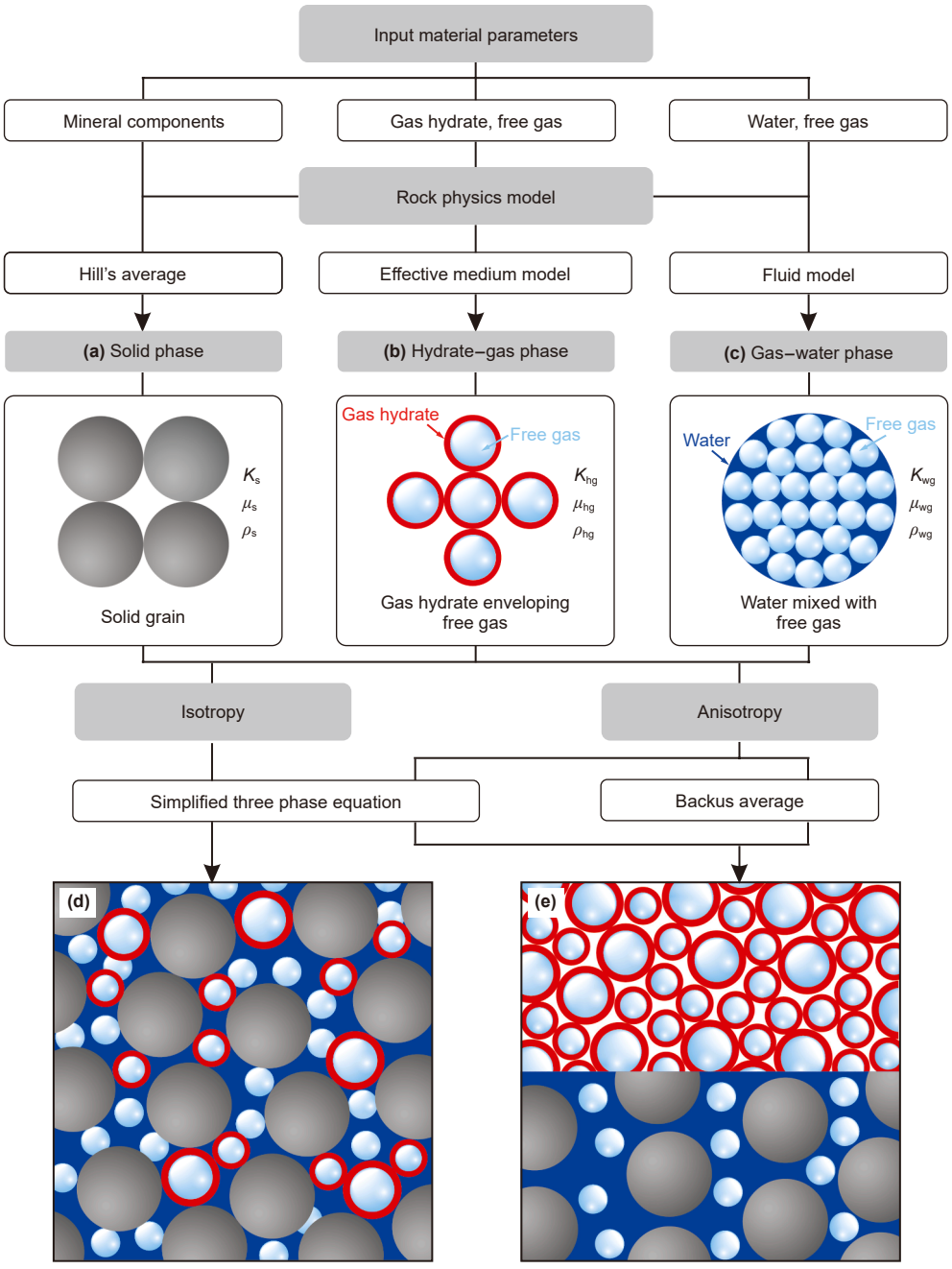

Fig. 2. Schematic diagrams and calculation flow for the coexistence model of hydrate–gas–water (CMHGW).

2009) and electrical properties (Cook et al., 2010). Based on the three-phases assumption that the sediments consist of solid phase (Fig. 2(a)), hydrate–gas phase (Fig. 2(b)), and gas–water phase (Fig. 2(c)), we develop isotropic (Fig. 2(d)) and anisotropic (Fig. 2(e)) models for the hydrate and free gas-coexisting sediments respectively. When the gas saturation is 0, our isotropic model is equivalent to the traditional STPE for pore-filling hydrate. In the model, a smaller value of the weakening parameter ε indicates a greater consolidation effect of hydrates on sediments (Lee and Collett, 2009). Therefore, as the parameter ε increases, the hydrate morphology will gradually transition from the grain-coating and cementing modes to load-bearing and fluid-filling modes. The parameter ε used in the model is closer to the load-bearing model in the EMT (Ecker et al., 1998, 2000; Dai et al., 2004; Qian et al., 2014, 2017). Our anisotropic model with a gas saturation of 0 is equivalent to the traditional two-layer model for fracture-filling hydrate.

2.1. Velocity model

In general, hydrates increase the sediment velocity, while free gas decreases the velocity (Lee and Collett, 2006; Liu et al., 2023; Zhu et al., 2024), providing the basis for simultaneously determining their saturations using velocity log data. In the velocity model, the hydrate-gas phase is described from the EMT (Dvorkin et al., 1999b). The STPE (Lee, 2008) is applied to combine the different phases including solid, hydrate–gas, and gas–water.

2.1.1. Isotropic velocity model

In the isotropic velocity model (Fig. 2(d)), the hydrate–gas phase is assumed to be uniformly distributed (Fig. 2(b)). Its bulk (K_{hg}) and shear (μ_{hg}) moduli are calculated using the Gassmann equation:

$$K_{hg} = K_h \frac{\phi_{g-hg} K_{h-dry} - \left(1+\phi_{g-hg}\right) K_g K_{h-dry} \big/ K_h + K_g}{\left(1-\phi_{g-hg}\right) K_g + \phi_{g-hg} K_h - K_g K_{h-dry} \big/ K_h}, \qquad (1)$$
$$\mu_{hg} = \mu_{h-dry};$$

where the subscripts h and g refer to hydrate and gas, respectively. ϕ_{g-hg} is gas porosity in the hydrate-gas phase. K_h, K_{h-dry} and μ_{h-dry} are the bulk moduli, the effective bulk and effective shear moduli of hydrate, respectively. K_g is the bulk moduli of gas. K_{h-dry} and μ_{h-dry} are computed from Eq. (2) (Dvorkin et al., 1999b):

The moduli K_{sat} and μ_{sat} of the sediments (Fig. 2(d)) are calculated from Eq. (4) using the moduli K_{hg} of hydrate–gas phase (Fig. 2(b)) and the moduli K_{wg} of the gas–water phase (Fig. 2(c)).

$$K_{sat} = K_s(1-\beta_1) + \beta_1^2 K_1,$$
$$\mu_{sat} = \mu_s(1-\beta_2);$$
$$K_1 = \left[\frac{(\beta_1-\phi)}{K_s} + \frac{\phi_{wg}}{K_{wg}} + \frac{\phi_{hg}}{K_{hg}}\right]^{-1},$$
$$\beta_1 = \frac{\phi_1(1+\alpha)}{1+\alpha\phi_1}, \beta_2 = \frac{\phi_1(1+\gamma\alpha)}{1+\gamma\alpha\phi_1}, \gamma = \frac{1+2\alpha}{1+\alpha}, \qquad (4)$$
$$\phi_1 = \phi_{wg} + \varepsilon\phi_{hg}, \phi_{wg} = \left(1 - S_h - S_{g-hg}\right)\phi, \text{and}$$
$$\phi_{hg} = \left(S_h + S_{g-hg}\right)\phi;$$

$$K_{h-dry} = \left[\frac{\phi_{g-hg}\big/\phi_c}{K_{HM}+\frac{4}{3}\mu_{HM}} + \frac{1-\phi_{g-hg}\big/\phi_c}{K+\frac{4}{3}\mu_{HM}}\right]^{-1} - \frac{4}{3}\mu_{HM},$$
$$\mu_{h-dry} = \left[\frac{\phi_{g-hg}\big/\phi_c}{\mu_{HM}+\frac{\mu_{HM}}{6}\left(\frac{9K_{HM}+8\mu_{HM}}{K_{HM}+2\mu_{HM}}\right)} + \frac{1-\phi_{g-hg}\big/\phi_c}{\mu+\frac{\mu_{HM}}{6}\left(\frac{9K_{HM}+8\mu_{HM}}{K_{HM}+2\mu_{HM}}\right)}\right]^{-1} - \frac{\mu_{HM}}{6}\left(\frac{9K_{HM}+8\mu_{HM}}{K_{HM}+2\mu_{HM}}\right); \quad \phi_{g-hg} < \phi_c;$$
$$K_{h-dry} = \left[\frac{\left(\phi_{g-hg}-\phi_c\right)\big/(1-\phi_c)}{\frac{4}{3}\mu_{HM}} + \frac{\left(1-\phi_{g-hg}\right)\big/(1-\phi_c)}{K_{HM}+\frac{4}{3}\mu_{HM}}\right]^{-1} - \frac{4}{3}\mu_{HM}, \qquad (2)$$
$$\mu_{h-dry} = \left[\frac{\left(\phi_{g-hg}-\phi_c\right)\big/(1-\phi_c)}{\frac{\mu_{HM}}{6}\left(\frac{9K_{HM}+8\mu_{HM}}{K_{HM}+2\mu_{HM}}\right)} + \frac{\left(1-\phi_{g-hg}\right)\big/(1-\phi_c)}{\mu_{HM}+\frac{\mu_{HM}}{6}\left(\frac{9K_{HM}+8\mu_{HM}}{K_{HM}+2\mu_{HM}}\right)}\right]^{-1} - \frac{\mu_{HM}}{6}\left(\frac{9K_{HM}+8\mu_{HM}}{K_{HM}+2\mu_{HM}}\right); \quad \phi_{g-hg} \geq \phi_c;$$

where ϕ_c, with a value range of 0.36 to 0.40, represents the critical porosity. The moduli K_{HM}, μ_{HM} and effective pressure P are computed from Eq. (3):

$$K_{HM} = \left[\frac{n_1^2(1-\phi_c)^2\mu_h{}^2}{18\pi^2(1-\nu_h)^2}P\right]^{1/3},$$
$$\mu_{HM} = \frac{5-4\nu_h}{5(2-\nu_h)}\left[\frac{3n_1^2(1-\phi_c)^2\mu_h{}^2}{2\pi^2(1-\nu_h)^2}P\right]^{1/3}; \qquad (3)$$
$$P = \left(1-\phi_{g-hg}\right)(\rho_h - \rho_g)gh;$$

where n_1 is the contact number per hydrate taken as 8 to 9; ν_h and μ_h are the Poisson's ratio and shear modulus of hydrate, respectively; h is the meters below seafloor; g is gravity acceleration; ρ_g and ρ_h are the densities of gas and hydrate, respectively.

where the subscripts s and w refer to solid grain and water; ϕ is the total porosity. S_h and S_{g-hg} are hydrate and gas saturations of hydrate–gas phase, respectively. When S_{g-hg} is equal to zero, CMHGW is the same as the conventional mixture model of gas and water (Dvorkin et al., 1999a). The moduli K_s and μ_s of solid phase are calculated from Hill's average of each mineral component. K_{wg} is the bulk modulus of the gas–water phase, and two cases of uniform and patchy distributions of gas are considered respectively (Dvorkin et al., 1999a). ε is the weakening parameter. α is the consolidation parameter of the sediments and is defined as

$$\alpha_i \approx \alpha_0 (d_0/d_i)^{n_2} \qquad (5)$$

where d_i represents different depths of the well log data. α_0 and n_2 are derived from fitting the velocity in the hydrate-free sediments.

The final sediment velocities are calculated from Eq. (6):

$$
\begin{aligned}
&V_p = \sqrt{\left(K_{sat} + \frac{4}{3}\mu_{sat}\right)\Big/\rho_b},\\
&V_s = \sqrt{\mu_{sat}/\rho_b};\\
&\rho_b = \rho_s(1-\phi) + \rho_w\phi S_w + \rho_h\phi S_h + \rho_g\phi S_g,\\
&S_w = 1 - S_h - S_g,\\
&S_g = S_{g-hg} + S_{g-wg},
\end{aligned}
\tag{6}
$$

where ρ_w and S_w are the density and saturation of water, respectively; ρ_s is the density of the solid grain. Gas saturation S_g consists of gas in both hydrate–gas and gas–water phases.

2.1.2. Anisotropic velocity model

The hydrate-bearing sediments of fracture-filling without free gas can be equivalent to the periodic two-layered media (Lee and Collett, 2009). In the presence of free gas, the first layer is the fracture filled with hydrate–gas phase (Fig. 2(e)), and its elastic moduli (K_{hg} and μ_{hg}) can be given by Eqs. (1)–(3). The second layer is the phase filled with gas–water saturated sediments (Fig. 2(e)), and its elastic moduli (K_{swg} and μ_{swg}) can be calculated from Eq. (4) by setting ϕ_{hg} to zero. Here we consider only two cases of horizontal and vertical fractures, as the continuous information on the fracture dips are not available in the well log data. In the case of horizontal fractures, a vertically symmetric, transversely isotropic (VTI) medium can be used as the model to describe the elastic stiffness matrix of the sediments (Rüger, 1997). The elastic constants C_{11}, C_{33}, C_{13}, C_{44}, and C_{66} of the stiffness matrix can be calculated using the elastic moduli K and μ of the two layers and Backus average (Backus, 1962) as follows:

$$
\begin{aligned}
&M = K + 4\mu/3,\\
&C_{11}^{VTI} = \left\langle 4\mu\left(1-\frac{\mu}{M}\right)\right\rangle + \left\langle\frac{1}{M}\right\rangle^{-1}\left\langle 1-\frac{2\mu}{M}\right\rangle^2,\\
&C_{33}^{VTI} = \left\langle\frac{1}{M}\right\rangle^{-1},\\
&C_{13}^{VTI} = \left\langle\frac{1}{M}\right\rangle^{-1}\left\langle 1-\frac{2\mu}{M}\right\rangle,\\
&C_{44}^{VTI} = \left\langle\frac{1}{\mu}\right\rangle^{-1},\\
&C_{66}^{VTI} = \langle\mu\rangle,
\end{aligned}
\tag{7}
$$

where the brackets $\langle\cdot\rangle$ represent the volumetric weighted averages of the properties. The elastic velocities in the VTI media (Mavko et al., 2009) can be written as

$$
\begin{aligned}
&V_P^{VTI}(\theta) = \left(\frac{C_{33}\cos^2\theta + C_{11}\sin^2\theta + C_{44} + \sqrt{M(\theta)}}{2\rho}\right)^{1/2},\\
&V_{SV}^{VTI}(\theta) = \left(\frac{C_{33}\cos^2\theta + C_{11}\sin^2\theta + C_{44} - \sqrt{M(\theta)}}{2\rho}\right)^{1/2},\\
&V_{SH}^{VTI}(\theta) = \left(\frac{C_{66}\sin^2\theta + C_{44}\cos^2\theta}{\rho}\right)^{1/2},\\
&M(\theta) = \left[(C_{33}-C_{44})\cos^2\theta - (C_{11}-C_{44})\sin^2\theta\right]^2 + (C_{44}+C_{13})^2\sin^2 2\theta,
\end{aligned}
\tag{8}
$$

where ρ can be calculated using the density in Eq. (6). Here we use a right-hand rectangular Cartesian coordinate (x_1, x_2, x_3). In this system, the x_3-axis is oriented vertically upward, and the x_1-axis is directed horizontally to the right. During the well logging, the measured velocity propagates along the direction of the vertical borehole, and θ can be considered as the angle between the rotated new x_3-axis and the direction of the vertical borehole. These two directions are coincident in the VTI media, so the velocity $V^{VTI}(0^\circ)$ in Eq. (8) is the velocity perpendicular to the horizontal fractures measured in the borehole. Since there are both vertically (V_{SV}) and horizontally (V_{SH}) polarized directions in the S-wave, V_{SH} in Eq. (8) is taken as the calculated S-wave velocity assuming that the fracture plane is parallel to the motion of S-wave in the well logging (Lee and Collett, 2009).

In the case of vertical fractures, a horizontally symmetric, transversely isotropic (HTI) medium can be used as the model to describe the elastic stiffness matrix (Rüger, 1997). The elastic stiffness matrix of HTI media can be obtained by rotating that of VTI media in Eq. (7) by the Bond method (Auld, 1990), which is expressed as follows:

$$
\begin{aligned}
&M = K + 4\mu/3,\\
&C_{11}^{HTI} = \left\langle\frac{1}{M}\right\rangle^{-1},\\
&C_{33}^{HTI} = \left\langle 4\mu\left(1-\frac{\mu}{M}\right)\right\rangle + \left\langle\frac{1}{M}\right\rangle^{-1}\left\langle 1-\frac{2\mu}{M}\right\rangle^2,\\
&C_{13}^{HTI} = \left\langle\frac{1}{M}\right\rangle^{-1}\left\langle 1-\frac{2\mu}{M}\right\rangle,\\
&C_{66}^{HTI} = \left\langle\frac{1}{\mu}\right\rangle^{-1},\\
&C_{44}^{HTI} = \langle\mu\rangle.
\end{aligned}
\tag{9}
$$

The elastic velocities in the HTI media (Mavko et al., 2009) are written as

The velocity $V^{HTI}(0^\circ)$ in Eq. (10) is the velocity parallel to the vertical fractures measured in the borehole. V_{sh} is also used for HTI media.

2.1.3. Velocity model test

Fig. 3(a)–(c) show elastic velocities calculated with the CMGHW. The calculation parameters for water saturation, depth, porosity and clay content are 0.5, 269 m below seafloor (mbsf), 0.5 and 0.75, respectively. The other parameters are taken from Site GMGS6-SH2 in Table 1. In Fig. 3, the green lines represent that the model only has the hydrate–gas phase, while the gas saturation in the gas–water phase is set to 0. The red and blue lines represent that the model only has gas–water phase, while the gas saturation in hydrate–gas phase is set to 0. The results show that with the increase of gas saturation, the elastic velocities generally decrease, although the velocities vary significantly between different models (Fig. 3). For the isotropic case, when the gas saturation is less than 25%, the P-wave velocity of the hydrate–gas model lies between those of patchy and uniform gas–water model. When the gas saturation exceeds 25%, the P-wave velocity of the hydrate–gas model is greater than the two velocities of gas–water model. The S-wave velocity of hydrate–gas model is always greater than that of gas–water model (Fig. 3(a)). For the anisotropic velocities vertical to the fracture, when the gas saturation is less than 5%, the P-wave velocity of hydrate–gas model lies between those of patchy and uniform gas–water model. When the gas saturation exceeds 5%, the P-wave velocity of hydrate–gas model is obviously lower than two velocities of gas–water model. However, the S-wave velocity

$$V_P^{HTI}(\theta)=\left(\frac{C_{11}\sin^2\theta+C_{33}\cos^2\theta+C_{66}+\sqrt{\left(C_{11}\sin^2\theta+C_{33}\cos^2\theta+C_{66}\right)^2-4A(\theta)}}{2\rho}\right)^{1/2},$$
$$V_{SV}^{HTI}(\theta)=\left(\frac{C_{11}\sin^2\theta+C_{33}\cos^2\theta+C_{66}-\sqrt{\left(C_{11}\sin^2\theta+C_{33}\cos^2\theta+C_{66}\right)^2-4A(\theta)}}{2\rho}\right)^{1/2},$$
$$V_{SH}^{HTI}(\theta)=\left(\frac{C_{66}\sin^2\theta+C_{44}\cos^2\theta}{\rho}\right)^{1/2},$$
$$A(\theta)=\left(C_{11}\sin^2\theta+C_{66}\cos^2\theta\right)\left(C_{66}\sin^2\theta+C_{33}\cos^2\theta\right)-(C_{13}+C_{66})^2\sin^2\theta\cos^2\theta. \quad (10)$$

of hydrate–gas model is consistently lower than that of gas-water model (Fig. 3(b)). For the anisotropic velocities parallel to the fracture, the elastic velocities of hydrate-gas model are mostly lower than those of gas–water model (Fig. 3(c)). The above analysis indicates that hydrate–gas phase complicates the velocity model.

2.2. Resistivity model

In the resistivity model, it is assumed that both hydrate and gas have the same effect on the calculation of water saturation (S_w) because of their insulating properties. Therefore, within the coexisting layer, the resistivity-derived saturation using the Archie equation actually represents the total saturation of hydrate and gas (Collett and Ladd, 2000). Although resistivity saturation does not differentiate hydrate from gas, it can constrain the total saturation calculated from velocity data. We refer to gas ($S_{g-hg}+S_{g-wg}$) and hydrate (S_h) saturation as a total saturation (S_{tal}) and define it as

$$S_{tal\ (h,\ g-hg\ and\ g-wg)}=S_h+S_{g-hg}+S_{g-wg}=S_h+S_g=1-S_w. \quad (11)$$

2.2.1. Isotropic resistivity model

In the isotropic resistivity model, the Archie equation (Archie, 1942) is also used to calculate the saturation of sediments that contain both hydrate and gas. The theoretical resistivity of the sediment (R_t) is calculated using the water saturation (S_w) and the resistivity of water-saturated sediments (R_0):

$$R_t=\frac{R_0}{S_w^{n_3}},\quad R_0=FR_w,\quad F=\frac{a}{\phi^m}, \quad (12)$$

where a, m and n_3 are empirical parameters. The range of parameter n_3 is between 1.72 and 2.17. The Arp's formula (Arps, 1953) is used to calculate the water resistivity (R_w) at a temperature of T degree Celsius.

2.2.2. Anisotropic resistivity model

The anisotropic resistivity model uses the same two-layered media as the anisotropic velocity model in Fig. 2. In the fracture model, the resistivity perpendicular ($R_\perp$) and parallel ($R_\parallel$) to the fractures respectively reflect the resistivity of the laminated fracture in series and in parallel (Kennedy and Herrick, 2004; Lee and Collett, 2009; Cook et al., 2010). They can be expressed as follows:

$$R_\parallel=\frac{1}{V_1\frac{\phi_1^{m_1}}{a_1}+V_2\frac{\phi_2^{m_2}}{a_2}}R_w,\quad R_\perp=\frac{V_2\frac{\phi_1^{m_1}}{a_1}+V_1\frac{\phi_2^{m_2}}{a_2}}{\left(\frac{\phi_1^{m_1}}{a_1}\right)\left(\frac{\phi_2^{m_2}}{a_2}\right)}R_w, \quad (13)$$

where V_1, ϕ_1, a_1, m_1, V_2, ϕ_2, a_2, and m_2 are the volume, porosity and Archie parameters of two layers, respectively. The Archie parameters a_1 and m_1 for the fractures filled with hydrate–gas phase are 1 and 2, respectively. The Archie parameters a_2 and m_2 are obtained from the resistivity of the hydrate- and gas-free sediments (Lee and Collett, 2009). In the vertical borehole, the well logs measure the horizontal resistivity. For the VTI media, the tensor resistivity $R_{ij}^{VTI}(\theta)$ and horizontal component $R_{11}^{VTI}(0^\circ)$ are written as:

$$R_{ij}^{VTI}(\theta)=\begin{bmatrix}c&0&-s\\0&1&0\\s&0&c\end{bmatrix}\begin{bmatrix}R_\parallel&0&0\\0&R_\parallel&0\\0&0&R_\perp\end{bmatrix}\begin{bmatrix}c&0&s\\0&1&0\\-s&0&c\end{bmatrix},$$
$$R_{11}^{VTI}(0^\circ)=R_\parallel,\quad c=\cos\theta,\quad s=\sin\theta, \quad (14)$$

when the formation is tilted by counterclockwise rotation along the x_2-axis. The parameter θ is also the angle between the rotated new x_3-axis and the direction of the vertical borehole. For the HTI media, the tensor resistivity $R_{ij}^{HTI}(\theta)$ and horizontal component $R_{11}^{HTI}(0^\circ)$ are written as:

$$R_{ij}^{HTI}(\theta)=\begin{bmatrix}c&0&-s\\0&1&0\\s&0&c\end{bmatrix}\begin{bmatrix}R_\perp&0&0\\0&R_\parallel&0\\0&0&R_\parallel\end{bmatrix}\begin{bmatrix}c&0&s\\0&1&0\\-s&0&c\end{bmatrix},$$
$$R_{11}^{HTI}(0^\circ)=R_\perp,\quad c=\cos\theta,\quad s=\sin\theta. \quad (15)$$

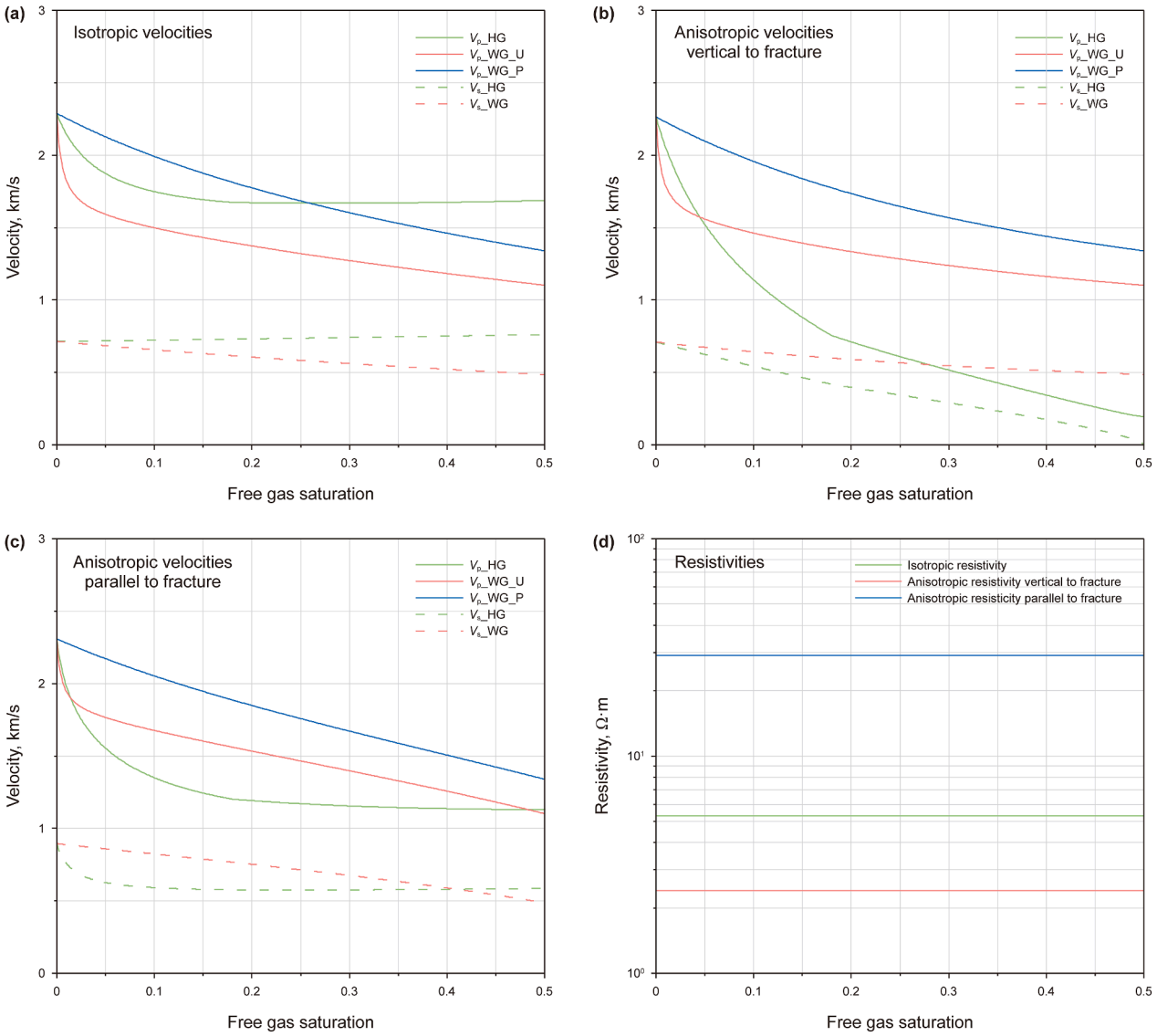

Fig. 3. Elastic velocities and resistivities calculated with the CMHGW. HG: hydrate–gas model; WG: water–gas model; U: uniformly distributed gas; P: patchily distributed gas.

Table 1
Calculation parameters. SSCS: southern South China Sea.

Expedition	Site	EMT		STPE				Archie equation							Geotherm	
		ϕ_c	n_1	α_0	d_0	n_2	ε	a	a_1	a_2	m	m_1	m_2	n_3	T_{sf}, °C	G_{geo}, °C/km
GMGS6	SH2	0.38	8	58	71	0.82	0.30	1.01	—	—	2.55	—	—	1.72	4.78	44.3
ODP 164	995	0.38	8	55	151	0.65	0.12	1.10	—	—	2.70	—	—	1.94	3.00	38.5
IODP 314	C0002	0.38	8	220	70	1.35	0.12	0.53	—	—	3.40	—	—	1.72	2.41	39.0
SSCS	DC_E	0.38	8	65	66	0.33	—	—	1	0.87	2.35	2	2.35	—	4.60	63.0
ODP 204	1250	0.38	8	110	73	0.60	—	—	1	1.13	2.20	2	2.20	—	3.99	58.0
IODP 311	U1328	0.38	8	110	75	0.60	—	—	1	3.68	0.50	2	0.50	—	3.50	54.0

2.2.3. Resistivity model test

Fig. 3(d) shows resistivities calculated using the CMGHW. The calculation parameters are consistent with the above velocity model. In Fig. 3(d), the green line represents the isotropic case, while the red and blue lines represent the cases vertical to and parallel to the fractures, respectively. In Fig. 3(d), the water saturation remains constant, and the hydrate saturation decreases as the gas saturation increases. However, since both hydrates and free gas are insulators, it can be observed that the resistivities in each case remain unchanged as the gas saturation increases. Nevertheless, the resistivities parallel to fractures are much higher than those vertical to fractures and those in the isotropic case.

2.3. Calculation flow

Four sets of well logs are used to calculate hydrate and gas saturations, including resistivity, P- and S-wave velocities, and density (Figs. 4–9). Density is used to derive porosity and correct the difference between water and hydrate. The grain density is 2.65 g/cc at Sites GMGS6-SH2, C0002 and DC_E, 2.70 g/cm^3 at Sites

995 and 1250 (Shipboard Scientific Party, 1996, 2003), and 2.75 g/cm^3 at Site1328 (Expedition 311 Scientists, 2006b). Due to the large density variation in the gas-bearing interval, density log data are not reliable for calculating an accurate porosity of the coexistence interval. Therefore, a linear or quadratic polynomial relationship between the density porosity and depth is used to fit the formation porosity (Figs. 4(b), 5(b), 6(b), 7(b), 8(b), 9(b)). Assuming that the gamma ray values of the shale-free zone and the shale beds are 10 API and 120 API respectively (Lee and Collett, 2009), the clay contents are obtained through the gamma ray measurements (Shipboard Scientific Party, 1996; Expedition 314 Scientists, 2009; Paganoni et al., 2016; Ye et al., 2020). From the clay content and porosity, the elastic modulus and densities of the solid phase, hydrate–gas phase, and gas–water phase are calculated using Hill's average, EMT and fluid models (Fig. 2(a)–(c)). Velocities, resistivities and densities of different saturations in isotropic and anisotropic media are then calculated in conjunction with the STPE, Backus average and resistivity model. The calculated values can be compared with actual logging measurements and the error is expressed by Eq. (16):

$$\mathrm{error}_{\min} = \sum_{i=0}^{4} \left(u_i^{\mathrm{m}} - u_i^{\mathrm{cal}}\right)^2, \tag{16}$$

where the superscripts m and cal refer to the actual measured value and the theoretical calculated value respectively. In the calculation, it is assumed that the saturations with the smallest error are the optimal solution. The density well logs are also used to verify gas saturation at Sites GMGS6-SH2, 1250, and U1328. In gas-bearing sediments, the measured density values tend to decrease, thereby providing a basis for deriving gas saturation using density. In hydrate–gas coexisting sediments, the density consists of solid grains, hydrates, gas and water, as shown in the density expression in Eq. (6). Assuming the same density for hydrate and water, their average $\overline{\rho}_{\mathrm{wh}}$ is used to rewrite Eq. (6):

$$\rho_{\mathrm{b}} = \rho_{\mathrm{s}}(1-\phi) + \overline{\rho}_{\mathrm{wh}}\phi(1-S_{\mathrm{g}}) + \rho_{\mathrm{g}}\phi S_{\mathrm{g}}, \tag{17}$$

The density-derived gas saturation can be written as:

$$S_{\mathrm{g}} = \frac{\rho_{\mathrm{s}}(1-\phi) + \overline{\rho}_{\mathrm{wh}}\phi - \rho_{\mathrm{b}}}{(\overline{\rho}_{\mathrm{wh}} - \rho_{\mathrm{g}})\phi}. \tag{18}$$

In Eq. (18), ϕ is obtained by fitting the background porosities of the water-saturated sediments.

The detailed calculation parameters for each site are shown in Table 1. They ensure that the calculation process is perturbed near the background values and improve the accuracy of saturations. The critical porosity ϕ_{c} and the average number of contacts per grain n (Helgerud et al., 1999) are set to be 0.38 and 8, respectively. The parameter d_0 is the initial depth of the well logs. The consolidation parameter α_0, exponent n_2, weakening parameter ε can be estimated using velocities of water-saturated sediments (Lee, 2006). The weakening parameter ε is usually recommended to be 0.12 for hydrate-bearing sediments (Lee, 2008). However, if the parameter ε of 0.12 is used at Site GMGS6-SH2, the predicted hydrate saturations are significantly lower than those estimated from the chlorinity. Therefore, we used the value of ε as 0.3. In the resistivity model, the Archie constants a and m are equal to a_2 and m_2 respectively. They can be derived by a crossplot of $\lg(R_0/R_{\mathrm{w}})$ against $\lg(\phi)$ of the hydrate- and gas-free sediments, in which the intercept and slope of the curve are $\lg(a)$ and m, respectively. The parameters a_1 and m_1 are set to be 1 and 2 respectively (Lee and Collett, 2012). The seafloor temperature and geothermal gradient of each site are respectively cited from the literatures (Guerin et al., 1999; Shipboard Scientific Party, 2003; Expedition 311 Scientists, 2006b; Miyakawa et al., 2014; Paganoni et al., 2016; Qian et al., 2018). The elastic constants of minerals and fluid components are from Lee and Collett (2006).

3. Results

The resistivity image and core data show that the hydrate morphology is pore-filling at Sites GMGS6-SH2, ODP 164 Site 995 and IODP 314 Site C0002 (Shipboard Scientific Party, 1996; Expedition 314 Scientists, 2009; Ye et al., 2020), and is fracture-filling at Sites DC_E, ODP 204 Site 1250 and IODP 311 Site 1328 (Paganoni et al., 2016; Shipboard Scientific Party, 2003; Expedition 311 Scientists, 2006b). Therefore, the isotropic model of CMHGW is applied to the Sites GMGS6-SH2, 995 and C0002, and the anisotropic model of CMHGW is applied to the Sites DC_E, 1250 and 1328.

3.1. Coexistence of pore-filling hydrate and gas

3.1.1. Site GMGS6-SH2

Site GMGS6-SH2, approximately 230 m from the GMGS3-W17, is located within the hydrate production test zone, offshore China (Qin et al., 2020). The logging data from these two sites are characterized by a two-layer structure (Qian et al., 2018). The two layers are distinguished by high resistivity, but their velocity and density characteristics exhibit significant differences. The overlying layer is a hydrate layer with high elastic velocity and little density variation. The underlying layer is a hydrate and gas coexisting layer with slightly high S-wave velocity, low P-wave velocity and low density (Fig. 4(a) and (b)). Using the seafloor temperature and geothermal gradient of Site GMGS3-W17 (Qian et al., 2018) and the water depth of 1242 m (Zhan et al., 2022), the I-BHSZ at Site GMGS6-SH2 is calculated to be 249 mbsf. Therefore, the depths of the overlying and underlying layers of this site range from 207 to 249 mbsf and 249 to 282 mbsf, respectively.

Based on the two gas models of uniform distribution and patchy distribution, Fig. 4(c) and (d) shows hydrate saturations (S_{h}) and gas saturations (S_{g}) calculated using CMHGW, respectively. S_{g} includes the total volume of gas both enveloped by hydrate ($S_{\mathrm{g-hg}}$) and mixed with water ($S_{\mathrm{g-wg}}$). S_{h} estimated from chlorinity data are also plotted in Fig. 4(c). As shown in Fig. 4(c) and (d), the calculated saturations are consistent with the two-layer structure of the well logs. The overlying layer can be considered to be a hydrate layer, as S_{g} is close to zero (Fig. 4(d)). The calculated S_{h} are the same for the two gas distribution models, with values ranging from 0 to 55%. In the underlying layer, S_{h} at a uniform distribution of free gas (red line in Fig. 4(c)) are approximately twice as high as those at a patchy distribution (blue line in Fig. 4(c)). The maximum S_{h} are present around the I-BHSZ, and S_{h} tend to decrease with depth. S_{h} at a patchy distribution of free gas are much closer to those derived from the chlorinity data (Fig. 4(c)), with smaller errors (Fig. 4(d)). On the contrary, S_{g} at a patchy distribution of free gas (blue line in Fig. 4(d)) are five times higher than those at a uniform distribution of free gas (red line in Fig. 4(d)), with maximum values of 30% and 6%, respectively. S_{g} at the patchy gas distribution is much closer to those derived from the measured density well data (Fig. 4(d)). Therefore, both hydrate and gas saturations indicate that free gas exhibits a patchy distribution within the hydrate and gas coexisting layer at Site GMGS6-SH2.

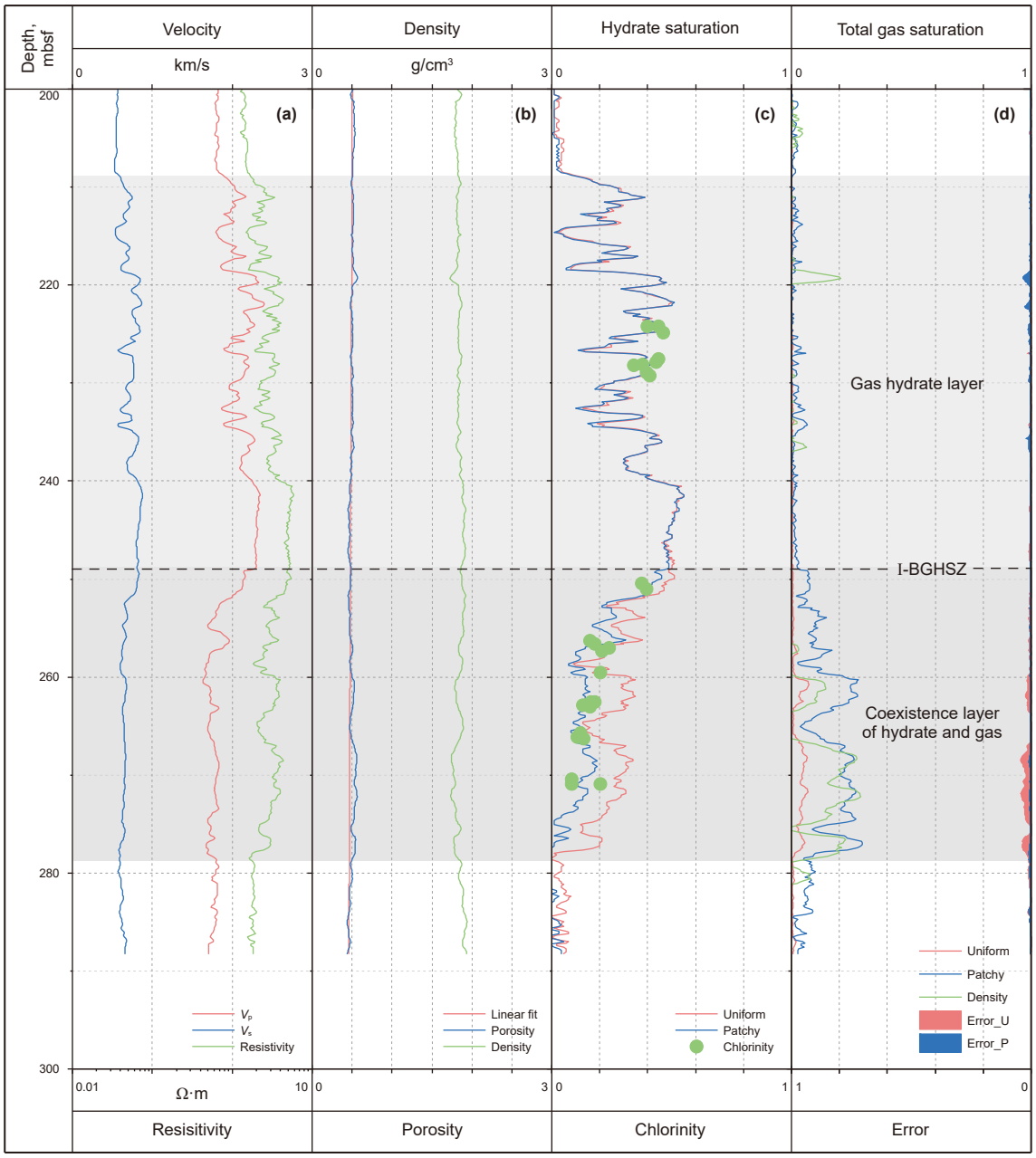

Fig. 4. **(a)**, **(b)** Well log data at Site GMGS6-SH2 (Qin et al., 2020). The porosities are derived from the densities. The red line in Fig. 4(b) represents the linearly fitted porosity. **(c)** Hydrate saturation (S_h). **(d)** Total gas saturation (S_g) and errors. Green points in Fig. 4(c) are the S_h estimated from chlorinity data. Green line in Fig. 4(d) represents the S_g calculated from density log data. Two horizontal axes are used to display different types of curves. U: uniformly distributed gas, P: patchily distributed gas.

3.1.2. Site 995

Site 995 penetrates the BSR and the I-BGHSZ at 440 and 520 mbsf respectively. Well log data show that the layer from 200 to 440 mbsf above the BSR is a hydrate layer. High resistivity is a distinct feature of this layer, while the elastic velocities and density are relatively stable. Between the two depths of the BSR and the I-BGHSZ, resistivity rapidly returns to the background value, while the P-wave velocity slightly decreases. The above two-layer structure is not well represented in the S-wave velocity and density (Fig. 5(a) and (b)). However, the saturations derived from the pressure cores below the BSR (Guerin et al., 1999) confirmed that hydrate and gas coexist at a depth of 493 mbsf (Fig. 5(c) and (d)).

Fig. 5(c) and (d) shows S_h and S_g calculated from well log data and pressure cores. It can be found that S_h above and below the BSR are generally close in two gas distribution models, and are also consistent with those from pressure cores. Above the BSR, S_h are not greater than 20% and S_g are close to 0, indicating a hydrate layer. Below the BSR, most of S_h and S_g are below 10% and close to those derived from pressure cores, indicating that hydrate and gas indeed coexist within this layer. In Fig. 5(d), S_g calculated from well logs with a patchy distribution are much closer to those derived from the pressure cores. A positive correlation between the density porosities and the errors can be observed in Fig. 5(c) and (d), indicating that the quality of the porosity log data affects the saturation accuracy.

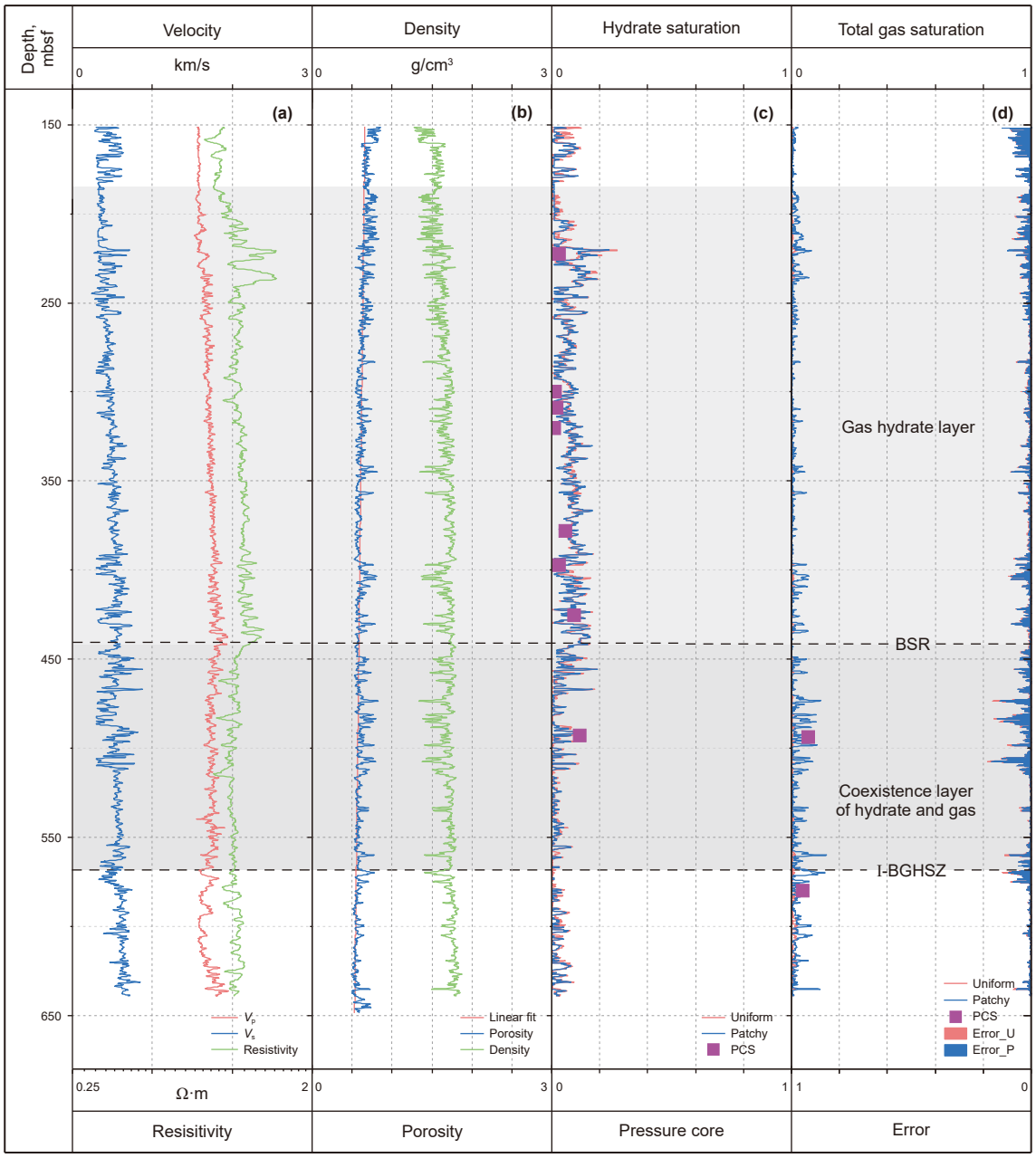

Fig. 5. **(a)**, **(b)** Well log data in ODP 164 Hole 995B. The porosities are derived from the densities. The red line in Fig. 5(b) represents the linearly fitted porosity. **(c)** Hydrate saturation (S_h). **(d)** Total gas saturation (S_g) and errors. Pink points in Fig. 5(c) and d are S_h and S_g derived from pressure cores, respectively (Guerin et al., 1999). Two horizontal axes are used to display different types of curves.

3.1.3. Site C0002

At Site C0002, core analysis indicated that hydrates are distributed in porous sand sediments (Moore et al., 2013). Although S-wave velocity is absent, the two-layer structure described above is evident in the P-wave velocity and resistivity responses. The BSR is located at ~400 mbsf with a double BSR and sII hydrates below (Taladay and Moore, 2015). In the overlying hydrate layer from 218.1 to 400.4 mbsf (Expedition 314 Scientists, 2009), the P-wave velocities and resistivities are high, and the densities increase slowly with local sharp decreases (Fig. 6(a) and (b)). Hydrates coexist with gas at several depths above the BSR from 309 to 321 mbsf (Miyakawa et al., 2014). The underlying potential gas layer between 481.6 and 547.1 mbsf exhibits a decrease in P-wave velocities and densities, and relatively high resistivities.

Fig. 6(c) and (d) shows the calculated S_h and S_g. The S_h derived from the chlorinity data in Holes C0002B, 2D, 2J, 2K, 2L (Moore et al., 2013) are also plotted in Fig. 6(c). The saturations show that S_h below the BSR are relatively close for the two different gas models, but S_g below the BSR in patchy model exceed those in uniform model. In addition to the layer from 309 to 321 mbsf, P-wave velocities and densities decrease above the BSR at 300, 343 and 376 mbsf (dark grey shaded areas in hydrate layer). Hydrates and gas are inferred to coexist at these depths because S_h varies between 20% and 40% while S_g are as high as 5% in the patchy model. Below the BSR, S_h are less than 20% and consistent with those calculated from chlorinity data, and S_g are up to 30%. The saturations of Site C0002 indicate that the coexistence occurs both above and below the BSR. In addition, the gas within our model is composed of two

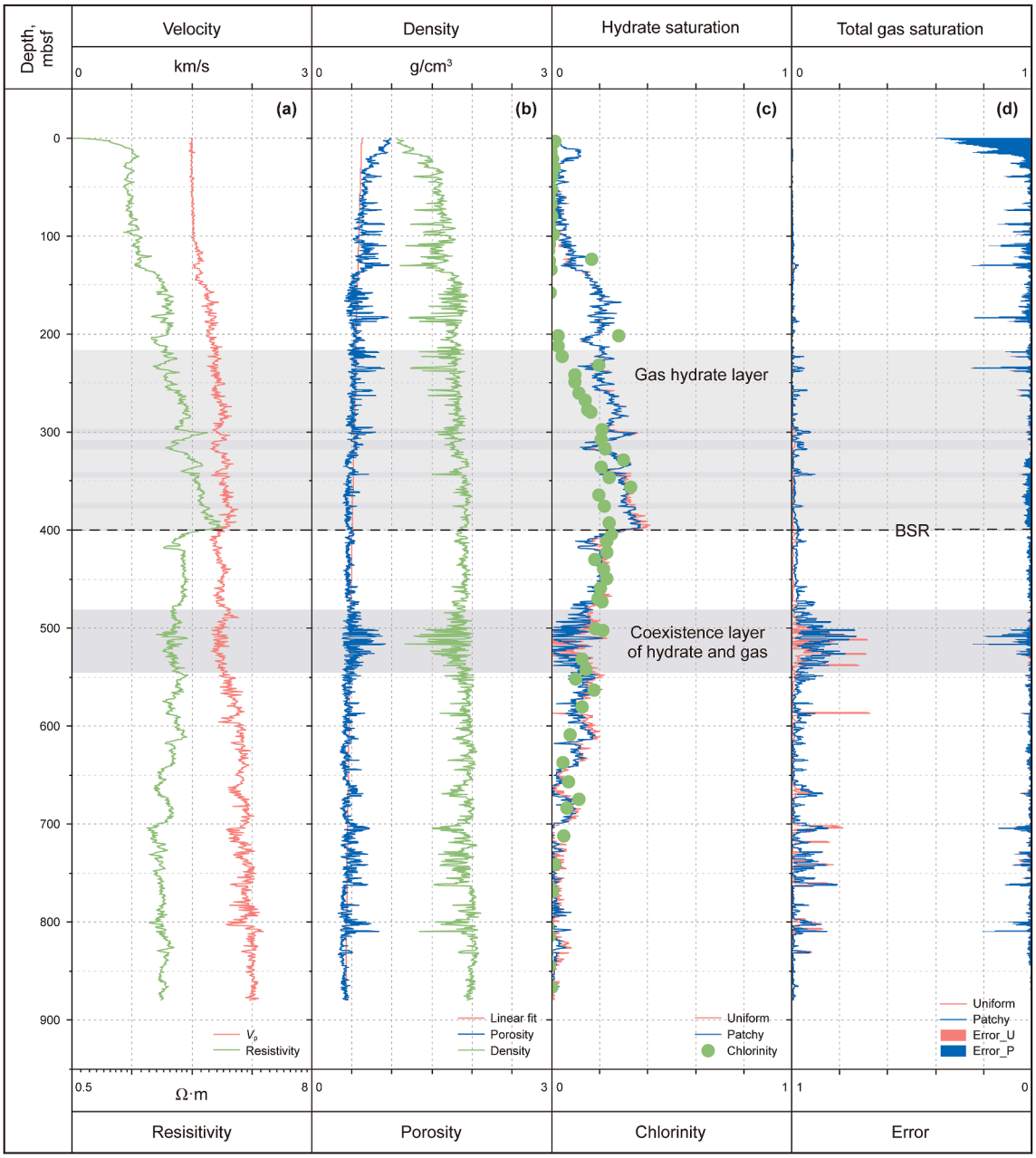

Fig. 6. **(a)**, **(b)** Well log data in IODP314 Hole C0002A. The porosities are derived from the densities. The red line in Fig. 6(b) is a quadratic polynomial fit to the density porosity. **(c)** Hydrate saturation (S_h). **(d)** Total gas saturation (S_g) and errors. Green points in Fig. 6(c) are the S_h estimated from chlorinity data in Holes C0002B, 2D, 2J, 2K, 2L (Moore et al., 2013). Two horizontal axes are used to display different types of curves.

components: one is the gas enveloped in hydrates, and the other is the gas mixed with water. There exist obvious discrepancies in the saturation calculations. However, the sum of the two components is comparatively close. This can explain why the total gas saturation calculated for the two gas distributions is relatively close in Fig. 6(d). Note that some larger errors (Fig. 6(d)) are caused by the significant local decreases in porosities, which are similar to those of the above Site 995.

3.2. Coexistence of fracture-filling hydrate and gas

3.2.1. Site DC_E

Both resistivity images and logging data at Site DC_E indicate that the hydrates are fracture-filling. Below the BSR, the cores and their gas compositions suggest that sII hydrates coexist with gas, accompanied by a double BSR on the seismic profile. The projected depths for the I-BSR or I-BGHSZ and the II-BGHSZ are ~153 and ~237 mbsf respectively (Paganoni et al., 2016). In general, density and S-wave velocity logs do not change much with depth, while resistivity and P-wave velocity logs are characterized by the two-layer structure (Fig. 7(a) and (b)). The overlying hydrate layer exhibits high resistivities and relatively high P-wave velocities. The underlying coexisting layer exhibits high resistivities but low P-wave velocities.

Fig. 7(c)–(f) shows the calculated S_h and S_g assuming vertical and horizontal fractures. S_h estimated from the cores are also plotted in Fig. 7(c) and (e). The calculated S_h for the vertical fracture in Fig. 7(c) are close to those from chlorinity data and pressure

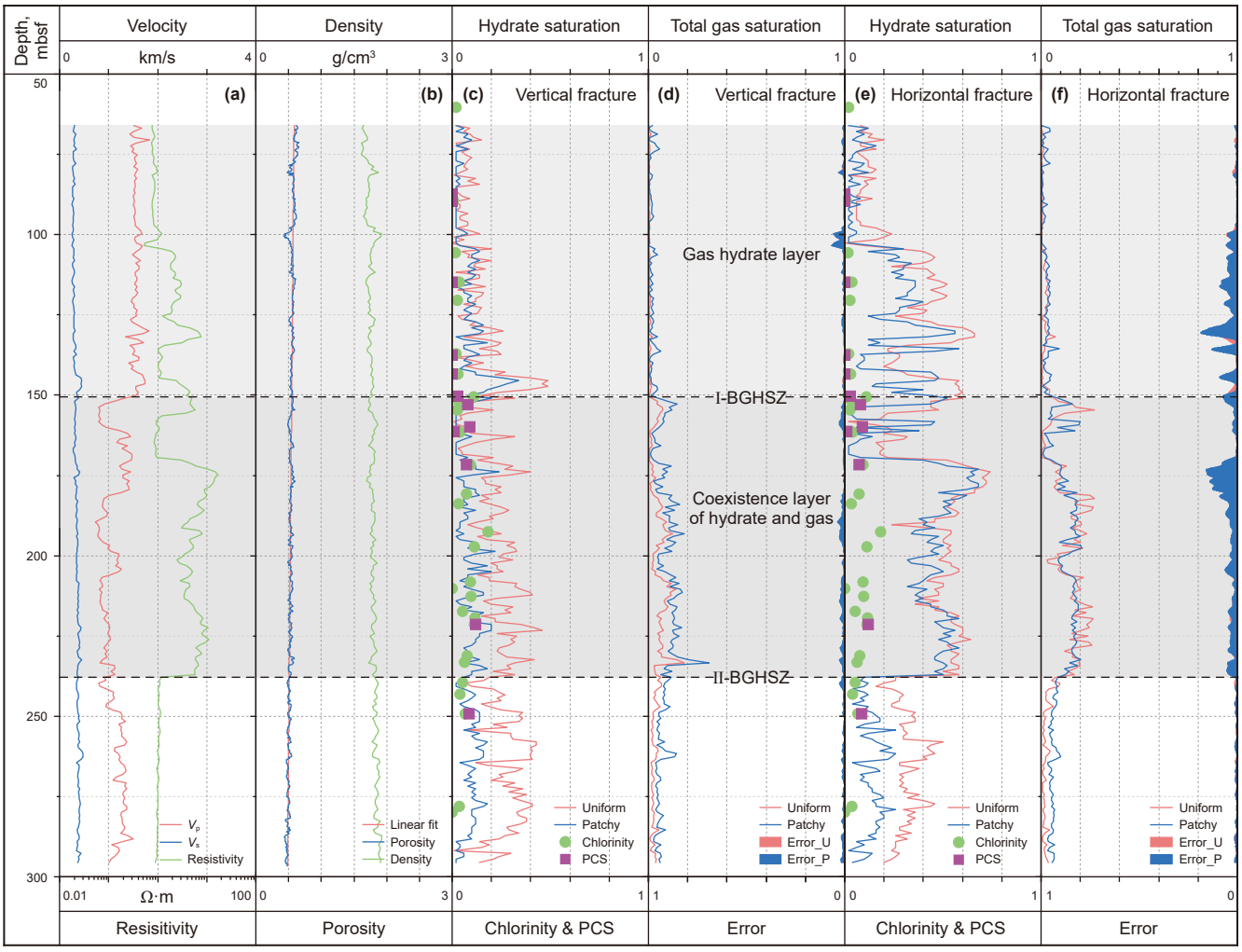

Fig. 7. **(a)**, **(b)** Well log data at Site DC_E (Paganoni et al., 2016). The porosities are derived from the densities. The red line in Fig. 7(b) represents the linearly fitted porosity. **(c)** Hydrate saturation (S_h), **(d)** total gas saturation (S_g) and errors calculated assuming a vertical fracture. **(e)** Hydrate saturation (S_h), **(f)** total gas saturation (S_g) and errors calculated assuming a horizontal fracture. Green and pink points are the S_h estimated from the cores.

cores, with small errors (Fig. 7(d)). The calculated S_h for the horizontal fracture in Fig. 7(e) are higher than those from the cores, with large errors (Fig. 7(f)). The saturations also support the fact that sub-vertical fractures are filled by hydrates. Assuming a vertical fracture, S_h at the patchy gas distribution are much closer to those estimated from the cores, with S_h mostly below 20% (Fig. 7(c)), slightly higher near the BSR, and S_g mostly below 20% (Fig. 7(d)). The saturations further suggest that Site DC_E has a two-layer structure consisting of an overlying hydrate layer and an underlying hydrate–gas coexisting layer. It can be found that the total gas saturations calculated by the two gas distribution models are relatively close (Fig. 7(d) and (f)). This is also because both of them represent the sum of the gas saturations of the two components in the model, similar to the case at Site C0002.

3.2.2. Site 1250

Site 1250 penetrates the BSR and a seismic Horizon A at ~114 and ~150 mbsf respectively. Core images show that hydrates in the sediments are mostly in the form of nodules and veins. sII hydrates were confirmed by the double BSRs on the seismic profile and heavy hydrocarbons in cores (Shipboard Scientific Party, 2003; Tréhu et al., 2003). The layer above the BSR exhibits high resistivity, relatively high P-wave velocity, stable S-wave velocity and density (Fig. 8(a) and (b)), indicating a hydrate layer. Between the BSR and horizon A, resistivity, velocity and density values are close to those of hydrate-free sediments. The above two-layer structure at Site 1250 is not obvious. However, gas probably (Shipboard Scientific Party, 2003) has induced the local density deductions above the BSR (dark grey shaded areas in Fig. 8).

Fig. 8(c)–(f) show the calculated S_h and S_g assuming vertical and horizontal fractures. S_h estimated from chlorinity data are low at this site and are shown in Fig. 8(c) and (e). It can be seen that S_h, assuming a vertical fracture and patchy gas distribution, are close to those derived from the chlorinity data, which are mostly around 10% (Fig. 8(c)). In Fig. 8(d), S_g approach zero but become relatively higher in regions with locally low densities. S_g at the patchy gas distribution is much closer to those derived from the measured density well data (Fig. 8(d)). Therefore, both hydrate and gas saturations indicate that free gas exhibits a patchy distribution within the hydrate and gas coexisting layer at Site 1250. At horizon A, the maximum S_g in the patchy gas distribution exceeds 10%, while S_h are approximately 20%, indicating a hydrate–gas coexisting layer.

3.2.3. Site U1328

At Site U1328, the inferred depth of the BSR is ~219 mbsf. Resistivity images above 50 mbsf show that the dips of the hydrate-

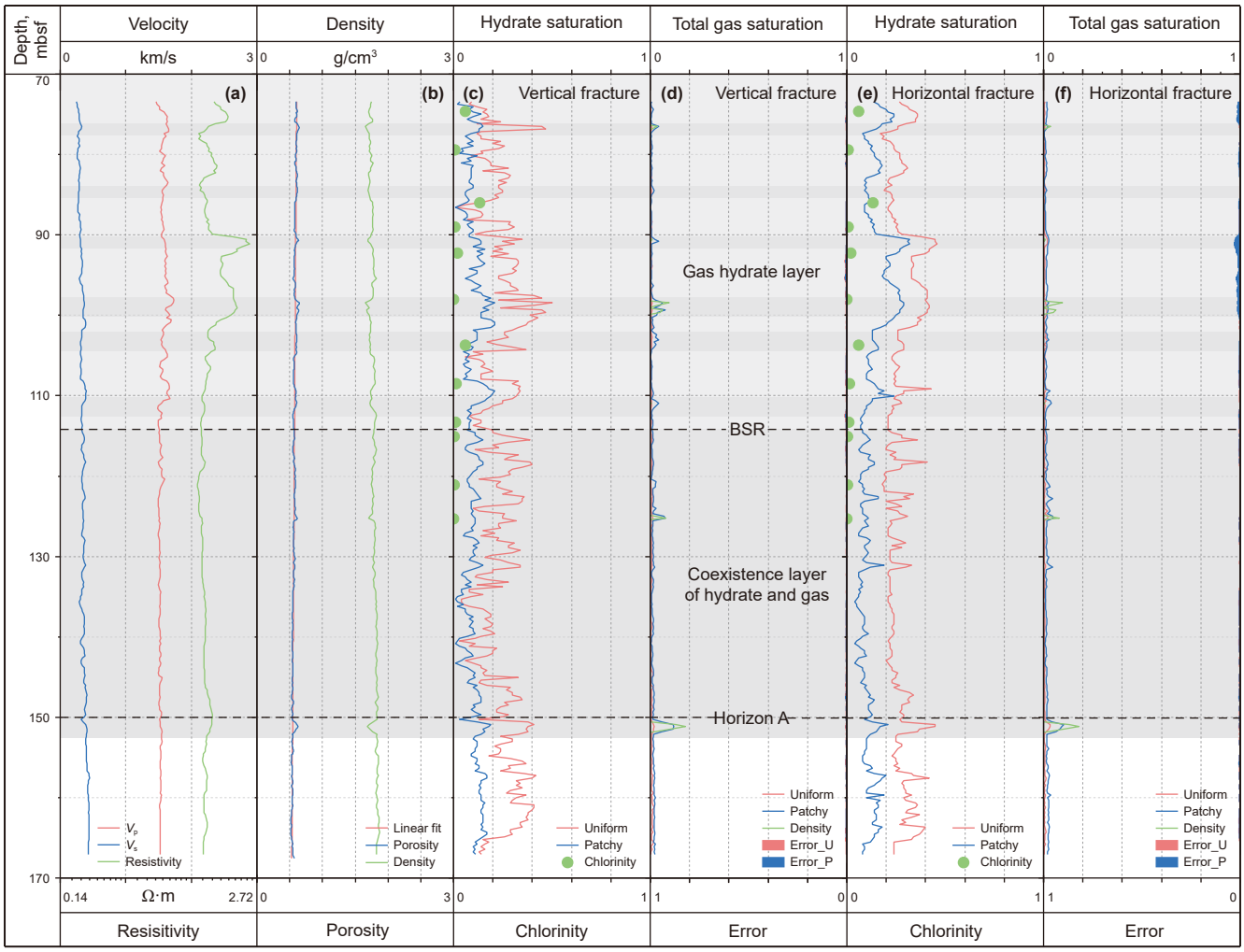

Fig. 8. **(a)**, **(b)** Well log data at ODP 204 Site 1250. The porosities are derived from the densities. The red line in Fig. 8(b) represents the linearly fitted porosity. **(c)** Hydrate saturation (S_h), **(d)** Total gas saturation (S_g) and errors calculated assuming a vertical fracture. **(e)** Hydrate saturation (S_h), **(f)** total gas saturation (S_g) and errors calculated assuming a horizontal fracture. Green lines in Fig. 8(d) and (f) represent S_g calculated from density log data. Green points are the S_h estimated from chlorinity data (Shipboard Scientific Party, 2003).

filled fractures are mostly at high angles. sII hydrates were indicated by the geochemical analyses of gas samples near the BSR (Expedition 311 Scientists, 2006a, 2006b). Due to the significant variation in the caliper above 130 mbsf, which compromises logging quality, only well log data below 130 mbsf are used in the calculation. Both velocity and resistivity log data are characterized by the two-layer structure. Velocity values are high above the BSR and low below it, while resistivity values are higher below the BSR than those above the BSR (Fig. 9(a)). Density log data are low at several depths (Fig. 9(b)), similar to those of Site 1250.

Fig. 9(c)–(f) shows the calculated S_h and S_g assuming vertical and horizontal fractures. In Fig. 9(c) and (e), S_h estimated from chlorinity data range from 7% to 43% and from a pressure core is 50% at 233 mbsf. Both in the cases of vertical and horizontal fractures, the calculated S_h from patchy gas distribution appear to be closer to those estimated from chlorinity data. However, at 202 and 233 mbsf, the calculated S_h from the horizontal fracture and uniform gas distribution are closer to those estimated from the cores. Except for 236 mbsf, at Site 1250, most of S_g are much closer to those derived from the measured density well data in the case of vertical hydrate fracture and patchy gas distribution (Fig. 9(d)). Both S_h and S_g are higher below the BSR than above it. Saturations indicate that hydrates coexist with gas in a thick layer below the BSR, and the coexistence even occurs locally above the BSR. Therefore, the hydrate morphology and gas distribution at Site 1328 are more complex, which may be the result of the active cold vent.

4. Discussions

4.1. Model applicability

In the evaluation of hydrates and free gas, core and well logging data can be used to predict their saturations. It is generally assumed that the saturations predicted by core data are relatively accurate in terms of depth and value range (Holland et al., 2019). Therefore, the prediction accuracy of the model can be verified by comparing the saturation derived from the core data with those calculated by the rock physics model. Through the calculation and comparison of the above six sites, it is found that the calculated saturations at Sites GMGS6-SH2, 995, and DC_E are highly accurate in both the hydrate and coexisting layers. Specifically, at Site 995, the calculated free gas saturations are very extremely close to the core-derived values. At Site C0002, the model-calculated and core-

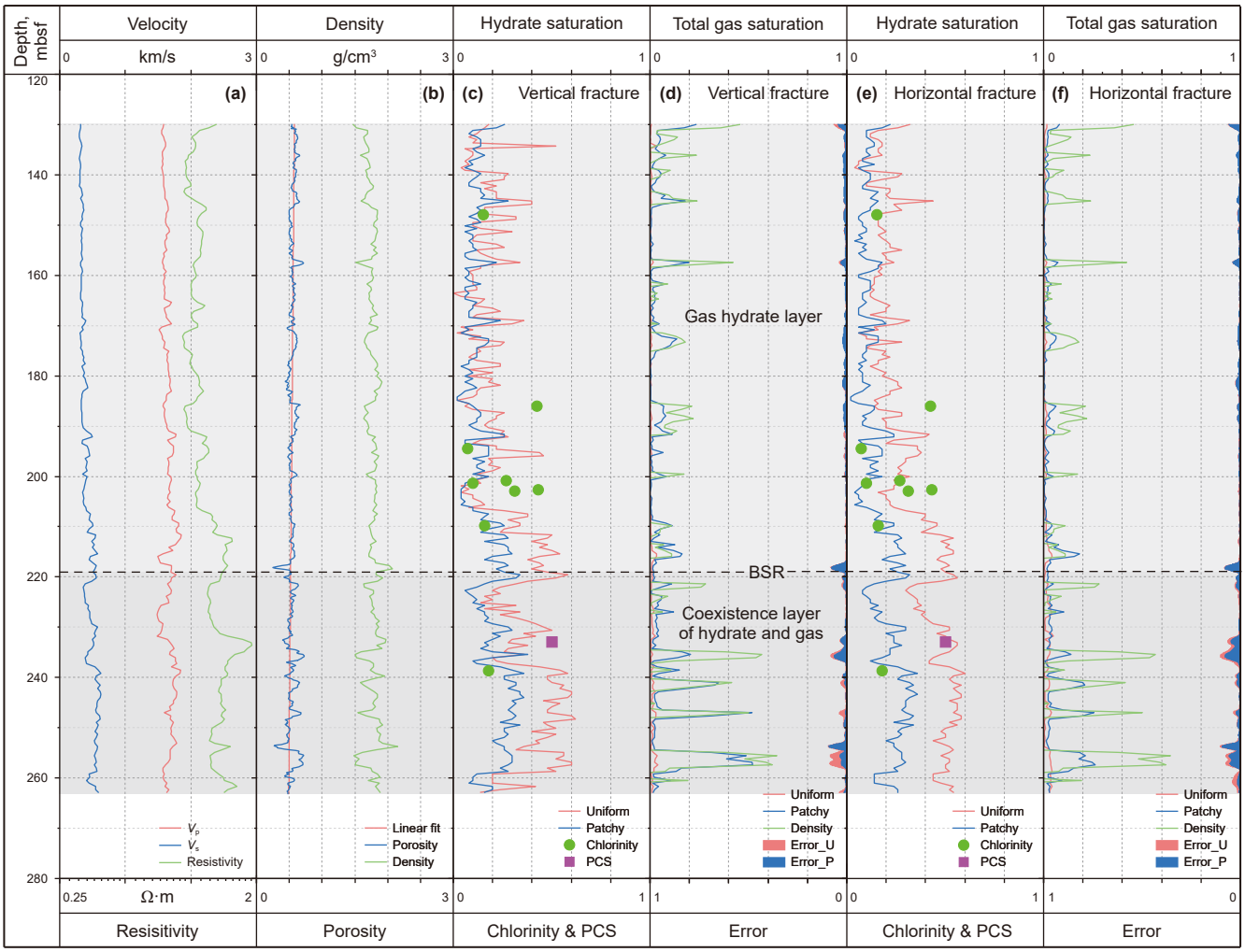

Fig. 9. **(a)**, **(b)** Well log data at IODP 311 Site 1328. The porosities are derived from the densities. The red line in Fig. 9(b) represents the linearly fitted porosity. **(c)** Hydrate saturation (S_h), **(d)** total gas saturation (S_g) and errors calculated assuming a vertical fracture. **(e)** Hydrate saturation (S_h), **(f)** total gas saturation (S_g) and errors calculated assuming a horizontal fracture. Green lines in Fig. 8(d) and (f) represent S_g calculated from density log data. Green and pink points are the S_h estimated from the cores (Expedition 311 Scientists, 2006b).

derived hydrate saturations are quite close in the coexisting layer, but there are discrepancies in the hydrate layer. This might be attributed to the fact that the cores and well logs are sourced from different holes (Expedition 314 Scientists, 2009).

However, at Sites 1250 and U1328, which are located in the cold seep areas with active fluids (Shipboard Scientific Party, 2003; Expedition 311 Scientists, 2006a), the calculation accuracy is relatively low. Gas hydrates, influenced by intense fluid activity, are characterized by a fracture-filling morphology. The dip and strike of hydrate fractures can affect the rock physics properties of the sediments (Cook and Goldberg, 2008; Cook et al., 2010). Due to the lack of continuous information on fracture dips and strikes, only vertical fracture and horizontal fracture are chosen for calculation within the model. This results in a reduction in the calculation accuracy of these two sites. In brief, the applicability of our model in isotropic pore-filling is higher than that in anisotropic fracture-filling. To improve the prediction accuracy in the anisotropic case, it is necessary to further enhance the resolution of the continuous fracture dip and strike information obtained from logging-while-drilling resistivity imaging and core scanning, and incorporate them into the model for calculation.

4.2. Comparison of CMHGW- and density-derived gas saturations

Eq. (18) is used to calculate the gas saturations at the above six sites. This method is found to be suitable for the sites where the density logs are smooth and decrease significantly in the gas-bearing interval, such as Sites GMGS6-SH2, 1250 and U1328 (Figs. 4, 8 and 9). At these three sites, the gas saturations derived from the density well log are close to those calculated from the model for the patchy gas distribution (Figs. 4(d), 8(d) and 9(d)). The comparison of two various gas saturations further validates the reliability of our new model CMHGW. This analysis also indicates that free gas in nature is likely to be predominantly characterized by the patchy distribution. However, the method of density-derived gas saturation is not suitable for the Sites 995 and C0002 with sharp variations in the well logs, or Site DC_E with no variations in the gas-bearing interval. Therefore, the density-

derived gas saturations are not shown at these three sites (Figs. 5–7).

4.3. Influencing factors on saturation calculations

4.3.1. Gas hydrate morphology

In the rock physics model, gas hydrate morphologies encompass grain-coating, cementing, load-bearing, fluid-filling, as well as nodules/fracture (Ecker et al., 1998, 2000; Dai et al., 2004). From the perspective of cores, Holland et al. (2008) classified the grain-coating, cementing, load-bearing and fluid filling with isotropic properties as pore-filling type, and designated the anisotropic nodules/fractures as fracture-filling type. Grain-coating and cementing models often occur in permafrost zones, and they can significantly increase the velocity of sediments; whereas load-bearing and fluid-filling types are usually found in shallow marine sediments, and they either increase or weakly increase the velocity of sediments (Dai et al., 2004; Collett et al., 2009). Therefore, when utilizing velocity well logs for saturation prediction, the first two models will yield either low hydrate saturation or high free gas saturation. Conversely, the latter two models will generate the opposite results. For isotropic marine sediments, the velocity values calculated by the load-bearing model in the pore-filling morphology are close to measured values (Ecker et al., 1998, 2000; Dai et al., 2004). Here we use the STPE, in which the sediment consolidation is characterized by the weakening parameter ε. A smaller weakening parameter ε corresponds to the more consolidated sediments. The parameter ε used in the model is equivalent to the load-bearing model in the EMT. In addition to loading-bearing model, Pan et al. (2020) attempted to predict hydrate saturation by means of a multi-model hybrid approach. In order to obtain a more precise hydrate saturation, the utilization of pressure cores for more accurate analysis of hydrate morphology should be a crucial direction in hydrate research.

4.3.2. Raw data quality

The quality of well logging and core data is crucial for the saturation calculation. The caliper log is one of the important indicators for measuring the quality of logging data. The quality of well logs at Sites GMGS6-SH2 and 1250 is high due to their stable caliper logs (Shipboard Scientific Party, 2003; Qin et al., 2020). At Sites 995, C0002, and U1328, the caliper logs with local drastic changes have affected the quality of the logging data, especially the density well log. Although the well logs have been corrected, sharp changes in density can still be seen on the logs (Guerin et al., 1999; Expedition 311 Scientists, 2006b; Expedition 314 Scientists, 2009). At Site DC_E, no caliper log is collected, but the quality of its velocity, resistivity, and density logs is high (Paganoni et al., 2016). To reduce the impact of caliper log on density and porosity, the fitted porosity is utilized in the model.

The quality of core data is susceptible to depth biases and artifacts, which will affect subsequent saturation predictions. The step changes in the gamma ray and density logs can be used to match the depths between core and log data (Bahk et al., 2013). During core collection, although advanced coring tools can reduce artifacts, core with severe impacts must be excluded during analysis (Holland et al., 2019).

4.3.3. Porosity

Density-derived porosity is one of the key parameters in the saturation calculations (Lee and Collett, 2009; Zhu et al., 2023). In Figs. 4–9, the density well logs at Sites GMGS6-SH2, DC_E, 1250 and U1328 are generally smooth, while those at Sites 995 and C0002 show significant local variations. At Sites 1250 and 1328, even within the HSZ, density values exhibit several local decreases. These decreases are induced by the presence of free gas (Shipboard Scientific Party, 2003), resulting in increases in density-derived porosities. Therefore, it is a challenge to derive the true porosities of the formation using density log data in the presence of decreased densities.

In this case, a linear or quadratic polynomial fitting is applied to the density-derived porosity to reduce the errors in the porosity calculation. To illustrate the effect of porosity, the velocities and resistivities under different porosities are modelled using the CMHGW and the calculated hydrate and gas saturations at 253 mbsf from Site GMGS6-SH2 (Fig. 4). In Fig. 10, the velocity and resistivity values decrease with increasing porosity. The above analysis in Fig. 3 also shows that as hydrate saturation decreases and gas saturation increases, the velocities decrease, while the resistivities remain unchanged. Hence, it is concluded that using higher porosities will result in lower hydrate saturation and higher gas saturation in calculations.

4.3.4. Parameters in velocity model

In the velocity model, the parameters α_0, d_0, n_2 and ε vary at these six sites. d_0 is the initial depth of the well logs, and it is a fixed value for each site. α_0, n_2 and ε need to be derived through fitting the velocities of background water-saturated sediments and the hydrate saturations. Therefore, their values are crucial to the calculation accuracy of the model. Based on the rock physics properties at Site GMGS6-SH2, Fig. 11(a)–(g) illustrates the velocity variation in relation to these three parameters. From Fig. 11(a)–(c), it can be observed that as α_0 increases from 0 to 50, the velocities decline sharply initially and subsequently tend to stabilize. This indicates that a low value of α_0 will lead to a low hydrate saturation or a high gas saturation. From Fig. 11(d)–(f), it can be seen that as n_2 increases from 0 to 2, the velocities exhibit an approximately linear increasing tendency. This implies that a high value of n_2 will result in a low hydrate saturation or a high gas saturation. At depicted in Fig. 11(g), the velocities exhibit a slight alteration when ε varies, indicating that α_0 and n_2 are two parameters within the model that are relatively sensitive to the velocities. In the anisotropic velocity model of two-layer media, since the hydrate saturation in the water-saturated sediments is 0, the velocities are not affected by the parameter ε, and the curves with a fixed velocity value are not plotted.

4.3.5. Parameters in resistivity model

Similar to the parameters α_0, n_2 and ε in the velocity model, the Archie constants a and m, along with the saturation exponent n_3, also need to be derived through fitting the background resistivity values of water-saturated sediments and hydrate saturations. Therefore, these three parameters will have an impact on the calculation accuracy of the model. Fig. 11(h) and (i) are the curves showing the variation of resistivity with parameters a, m, and n_3 under isotropic and anisotropic conditions, respectively. The resistivities increase linearly with the increase of parameter a, and increases exponentially with the increase of parameters m and n_3. The increasing trends of the resistivities are highly conspicuous, suggesting that these three parameters are very sensitive to the calculation of resistivity. These increasements signify mean that the high values of a, m, and n_3 will lead to a low hydrate saturation or a low gas saturation. In the anisotropic resistivity model of the two-layer media, the resistivities remain unaffected by the saturation exponent n_3, and the corresponding curves are also not plotted.

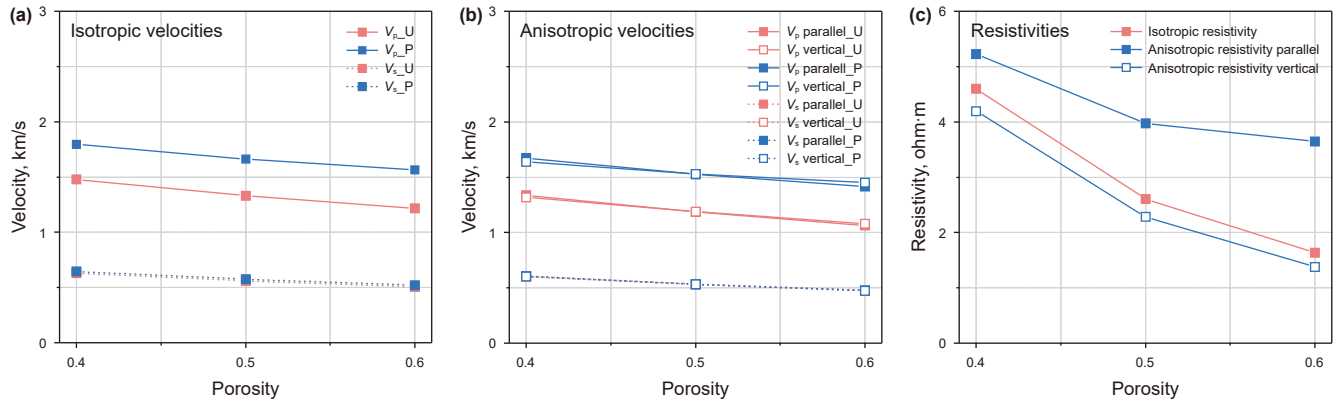

Fig. 10. Variation of velocity and resistivity with porosity. **(a)** Isotropic velocities; **(b)** anisotropic velocities; **(c)** resistivities. Parallel: parallel to fracture, Vertical: vertical to fracture. U: uniformly distributed gas, P: patchily distributed gas.

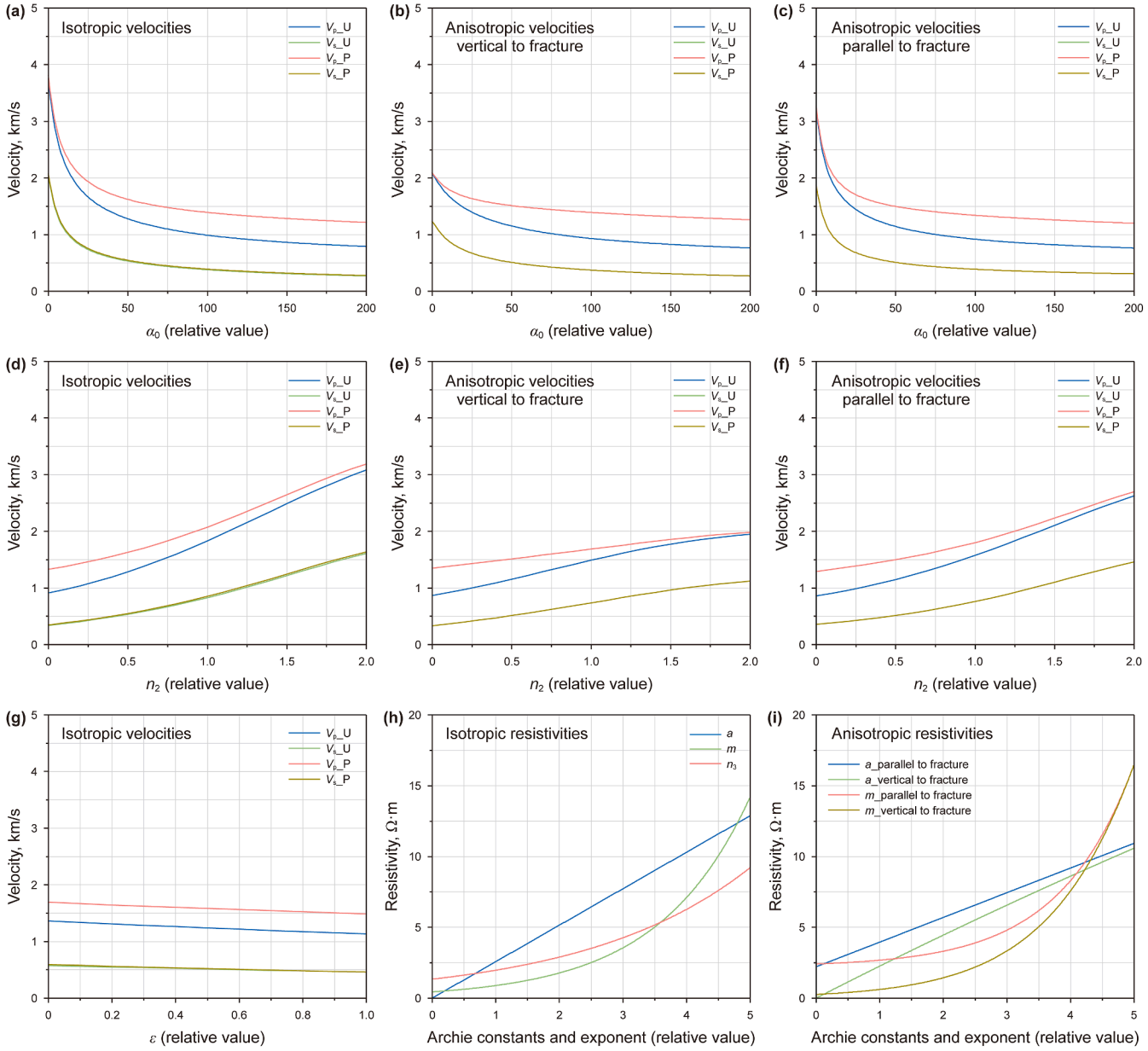

Fig. 11. Test of the calculation parameters. **(a)**–**(c)** Variation of velocities with α_0. **(d)**–**(f)** Variation of velocities with n_2. **(g)** Variation of velocities with ε. **(h)** and **(i)** Variation of resistivities with Archie constants and exponent.

5. Conclusions

A new rock physics model is developed for the multiphase mixing in marine hydrate and free gas-coexisting sediments. In the model, the sediments are composed of three phases: solid phase, hydrate–gas phase, and gas–water phase. The model is validated through saturation calculations at six marine sites worldwide. The calculated saturations closely match those derived from the cores, suggesting that our new model is suitable for predicting the saturations in the hydrate–gas coexisting layer.

Our results provide further evidence from a saturation perspective that hydrate–gas coexistence can occur both above and below the BSR. This coexistence is likely to be a neglected global phenomenon, and the saturation distribution would deepen our understanding of such a complex system. The underlying hydrate and gas, interpreted below the conventional I-BSR, would provide a more accurate prediction of global hydrate resources, potentially exceeding the current estimates.

CRediT authorship contribution statement

Jin Qian: Writing – original draft, Conceptualization. **Xiu-Juan Wang:** Resources. **Zhen Liu:** Validation, Software. **Qiao-Qiao Wang:** Visualization, Data curation. **Jia-Peng Jin:** Writing – review & editing, Investigation. **Neng-You Wu:** Supervision, Project administration.

Data availability statement

Data are available through Paganoni et al. (2016), Qin et al. (2020) and Lamont-Doherty (https://mlp.ldeo.columbia.edu/logdb), and can obtained from the corresponding author.

Declaration of interests

The authors declare that they have no known competing financial interests or personal relationships that could have appeared to influence the work reported in this paper.

Acknowledgements

We wish to thank ODP, IODP and the Borehole Research Group for providing us the original well logs and the core-derived saturations. We thank two anonymous reviewers for providing detailed comments and suggestions which have significantly improved the quality of the manuscript. This research is funded by DeepEarth Probe and Mineral Resources Exploration – National Science and Technology Major Project (No. 2024ZD1004201) and National Natural Science Foundation of China (42076072, 41676040 and 41276053).

References

Archie, G.E., 1942. The electrical resistivity log as an aid in determining some reservoir characteristics. Trans. AIMS 146 (1), 54–62. https://doi.org/10.2118/942054-G.

Arps, J.J., 1953. The effect of temperature on the density and electrical resistivity of sodium chloride solutions. Petrol. Tech. 5 (10), 17–20. https://doi.org/10.2118/953327-G.

Auld, B.A., 1990. Acoustic Fields and Waves in Solids, Vols. 1, 2. Robert E. Krieger Publication Co, Malabar, FL.

Backus, G.E., 1962. Long-wave elastic anisotropic produced by horizontal layering. J. Geophys. Res. 67 (11), 4427–4440. https://doi.org/10.1029/JZ067i011p04427.

Bahk, J.J., Kim, G.Y., Chun, J.H., et al., 2013. Characterization of gas hydrate reservoirs by integration of core and log data in the Ulleung basin, East Sea. Mar. Petrol. Geol. 47, 30–42. https://doi.org/10.1016/j.marpetgeo.2013.05.007.

Bohrmann, G., Greinert, J., Suess, E., et al., 1998. Authigenic carbonates from the Cascadia subduction zone and their relation to gas hydrate stability. Geology 26 (7), 647–650. https://doi.org/10.1130/0091-7613(1998)026<0647:ACFTCS>2.3.CO;2.

Collett, T.S., Ladd, J., 2000. Detection of gas hydrate with downhole logs and assessment of gas hydrate concentrations (saturations) and gas volumes on the Blake Ridge with electrical resistivity log data. Proc. Ocean Drill. Progr. Sci. Results 164, 179–191.

Collett, T.S., Johnson, A.H., Knapp, C.C., et al., 2009. Natural gas hydrates: A review. In: Collett, T., Johnson, A., Knapp, C., Boswell, R. (Eds.), Natural Gas hydrates—Energy Resource Potential and Associated Geologic Hazards, vol. 89. AAPG Memoir, pp. 146–219. https://doi.org/10.1306/M891320.

Cook, A.E., Anderson, B.I., Malinverno, A., et al., 2010. Electrical anisotropy due to gas hydrate-filled fractures. Geophysics 75 (6), F173–F185. https://doi.org/10.1190/1.3506530.

Cook, A.E., Goldberg, D., 2008. Extent of gas hydrate filled fracture planes: Implications for in situ methanogenesis and resource potential. Geophys. Res. Lett. 35 (15), L15302. https://doi.org/10.1029/2008GL034587.

Dai, J.C., Xu, H.B., Snyder, F., et al., 2004. Detection and estimation of gas hydrates using rock physics and seismic inversion: Examples from the northern deepwater Gulf of Mexico. Lead. Edge 23 (1), 60–66. https://doi.org/10.1190/1.1645456.

Dvorkin, J., Moos, D., Packwood, J.L., et al., 1999a. Identifying patch saturation from well logs. Geophysics 64 (6), 1756–1759. https://doi.org/10.1190/1.1444681.

Dvorkin, J., Prasad, M., Sakai, A., et al., 1999b. Elasticity of marine sediments: Rock physics modeling. Geophys. Res. Lett. 26 (12), 1781–1784. https://doi.org/10.1029/1999GL900332.

Ecker, C., Dvorkin, J., Nur, A., 1998. Sediments with gas hydrate: Internal structure from seismic AVO. Geophysics 63 (5), 1659–1669. https://doi.org/10.1190/1.1444462.

Ecker, C., Dvorkin, J., Nur, A., 2000. Estimating the amount of gas hydrate and free gas from marine seismic data. Geophysics 65 (2), 563–573. https://doi.org/10.1190/1.1444752.

Expedition 311 Scientists, 2006. Expedition 311 summary. In: Riedel, M., Collett, T.S., Malone, M.J. (Eds.), Proc. IODP, 311. Integrated Ocean Drilling Program Management International, Inc., Washington, DC. https://doi.org/10.2204/iodp.proc.311.101.2006

Expedition 311 Scientists, 2006. Site U1328. In: Riedel, M., Collett, T.S., Malone, M.J. (Eds.), Proc. IODP, 311. Integrated Ocean Drilling Program Management International, Inc., Washington, DC. https://doi.org/10.2204/iodp.proc.311.106.2006

Expedition 314 Scientists, 2009. Expedition 314 site C0002. In: Kinoshita, M., Tobin, H., Ashi, J., Kimura, G., Lallemant, S., Screaton, E.J., Curewitz, D., Masago, H., Moe, K.T. (Eds.), Proc. IODP, 314/315. Integrated Ocean Drilling Program Management International, Inc., Washington, DC. https://doi.org/10.2204/iodp.proc.314315316.114.2009

Guerin, G., Goldberg, D.S., Meltser, A., 1999. Characterization of in situ elastic properties of gas hydrate-bearing sediments on the blake ridge. J. Geophys. Res. 104 (B8), 17781–17795. https://doi.org/10.1029/1999JB900127.

He, Z.X., Zhang, F., Ding, P.B., et al., 2025. Analysis of seismic dispersion and attenuation for gas-hydrate formations in the South China Sea. Pet. Sci. 22 (8), 3279–3292. https://doi.org/10.1016/j.petsci.2025.05.008.

Helgerud, M.B., Dvorkin, J., Nur, A., et al., 1999. Elastic-wave velocity in marine sediments with gas hydrates: Effective medium modeling. Geophys. Res. Lett. 26 (13), 2021–2024. https://doi.org/10.1029/1999GL900421.

Holland, M., Schultheiss, P., Roberts, J., et al., 2008. Observed gas hydrate morphologies in marine sediments. In: Proceedings of the 6th International Conference on Gas Hydrates (ICGH 2008). Vancouver British Columbia, Canada. https://doi.org/10.14288/1.0041062.

Holland, M.E., Schultheiss, P.J., Roberts, J.A., 2019. Gas hydrate saturation and morphology from analysis of pressure cores acquired in the Bay of Bengal during expedition NGHP-02, offshore India. Mar. Petrol. Geol. 108, 407–423. https://doi.org/10.1016/j.marpetgeo.2018.07.018.

Jana, S., Ojha, M., Sain, K., 2015. Gas hydrate saturation from heterogeneous model constructed from well log in Krishna-Godavari Basin, Eastern Indian Offshore. Geophys. J. Int. 203 (1), 184–194. https://doi.org/10.1093/gji/ggv293.

Kennedy, W.D., Herrick, D.C., 2004. Conductivity anisotropy in shale-free sandstone. Petrophysics 45 (1), 38–58.

Kida, M., Khlystov, O., Zemskaya, T., et al., 2006. Coexistence of structure I and II gas hydrate in Lake Baikal suggesting gas sources from microbial and thermogenic origin. Geophys. Res. Lett. 33 (24), L24603. https://doi.org/10.1029/2006GL028296.

Klapp, S.A., Bohrmann, G., Kuhs, W., et al., 2010. Mixed gas hydrate structures at the Chapopote Knoll, southern Gulf of Mexico. Ear. Planet. Sci. Lett. 299 (1), 207–217. https://doi.org/10.1016/j.epsl.2010.09.001.

Kumar, D., Sen, M.K., Bangs, N.L., et al., 2006. Seismic anisotropy at hydrate Ridge. Geophys. Res. Lett. 33 (1), L01306. https://doi.org/10.1029/2005GL023945.

Kvenvolden, K.A., 1993. Gas hydrates—Geological perspective and global change. Rev. Geophys. 31 (2), 173–187. https://doi.org/10.1029/93RG00268.

Lee, M.W., 2006. A simple method of predicting S-wave velocity. Geophysics 71 (6), F161–F164. https://doi.org/10.1190/1.2357833.

Lee, M.W., 2008. Models for gas hydrate-bearing sediments inferred from hydraulic permeability and elastic velocities. US Geological Survey Scientific Investigations Report 2008–5219, 1–14. https://doi.org/10.3133/sir20085219.

Lee, M.W., Collett, T.S., 2006. Gas hydrate and free gas saturations estimated from velocity logs on Hydrate Ridge, offshore Oregon, U.S.A. In: Proc. Ocean Drill Prog. 199 Sci. Results, 204. Ocean Drilling Program, College Station, TX, pp. 1–25. https://doi.org/10.2973/odp.proc.sr.204.103.2006.

Lee, M.W., Collett, T.S., 2009. Gas hydrate saturations estimated from fractured reservoir at Site NGHP-01-10, Krishna-Godavari Basin, India. J. Geophys. Res. Solid Earth 114, B07102. https://doi.org/10.1029/2008JB006237.
Lee, M.W., Collett, T.S., 2011. In-situ gas hydrate saturation estimated from various well logs at the Mount Elbert Gas Hydrate Stratigraphic Test Well, Alaska North Slope. Mar. Petrol. Geol. 28, 439–449. https://doi.org/10.1016/j.marpetgeo.2009.06.007.
Lee, M.W., Collett, T.S., 2012. Pore- and fracture-filling gas hydrate reservoirs in the Gulf of Mexico Gas Hydrate joint industry project leg II green canyon 955 H well. Mar. Petrol. Geol. 34, 62–71. https://doi.org/10.1016/j.marpetgeo.2011.08.002.
Li, J.F., Ye, J.L., Qin, X.W., et al., 2018. The first offshore natural gas hydrate production test in South China Sea. China Geol. 1 (1), 5–16. https://doi.org/10.31035/cg2018003.
Liu, S.B., Han, T.C., Fu, L.Y., 2023. Laboratory insights into the effects of methane hydrate on the anisotropic joint elastic-electrical properties in fractured sandstones. Pet. Sci. 20 (2), 803–814. https://doi.org/10.1016/j.petsci.2022.09.007.
Lu, H.L., Seo, Y.T., Lee, J.W., et al., 2007. Complex gas hydrate from the cascadia margin. Nature 445 (7125), 303–306. https://doi.org/10.1038/nature05463.
Marín-Moreno, H., Sahoo, S.K., Best, A.I., 2017. Theoretical modeling insights into elastic wave attenuation mechanisms in marine sediments with pore-filling methane hydrate. J. Geophys. Res. Solid Earth 122 (2), 1835–1847. https://doi.org/10.1002/2016JB013577.
Mavko, G.M., Mukerji, T., Dvorkin, J., 2009. The Rock Physics Handbook. Tools for Seismic Analysis in Porous Media, second ed. Cambridge Univ. Press, New York. https://doi.org/10.1017/CBO9780511626753.
Milkov, A.V., Dickens, G.R., Claypool, G.E., et al., 2004. Co-existence of gas hydrate, free gas, and brine within the regional gas hydrate stability zone at hydrate ridge (Oregon margin): Evidence from prolonged degassing of a pressurized core. Earth Planet Sci. Lett. 222 (3), 829–843. https://doi.org/10.1016/j.epsl.2004.03.028.
Miyakawa, A., Saito, S., Yamada, Y., et al., 2014. Gas hydrate saturation at site C0002, IODP expeditions 314 and 315, in the Kumano Basin, Nankai trough. Isl. Arc 23 (2), 142–156. https://doi.org/10.1111/iar.12064.
Moore, G., Kanagawa, K., Strasser, M., et al., 2013. NanTroSEIZE stage 3: NanTroSEIZE plate boundary deep riser 2. IODP Prel. Rept. 338. https://doi.org/10.2204/iodp.pr.338.2013.
Paganoni, M., Cartwright, J.A., Foschi, M., et al., 2016. Structure II gas hydrates found below the bottom-simulating reflector. Geophys. Res. Lett. 43 (11), 5696–5706. https://doi.org/10.1002/2016GL069452.
Pan, H.J., Li, H.B., Chen, J.Y., et al., 2020. Quantification of gas hydrate saturation and morphology based on a generalized effective medium model. Mar. Petrol. Geol. 113, 104166. https://doi.org/10.1016/j.marpetgeo.2019.104166.
Pecher, I.A., Holbrook, W.S., Sen, M.K., et al., 2003. Seismic anisotropy in gas-hydrate- and gas-bearing sediments on the Blake Ridge, from a walkaway vertical seismic profile. Geophys. Res. Lett. 30 (14), 1733. https://doi.org/10.1029/2003GL017477.
Qian, J., Wang, X.J., Wu, S.G., et al., 2014. AVO analysis of BSR to assess free gas within fine-grained sediments in the Shenhu area, South China Sea. Mar. Geophys. Res. 35 (2), 125–140. https://doi.org/10.1007/s11001-014-9214-z.
Qian, J., Wang, X.J., Collett, T.S., et al., 2017. Gas hydrate accumulation and saturations estimated from effective medium theory in the eastern Pearl Mouth Basin, South China Sea. Interpretation 5 (3), SM38–SM48. https://doi.org/10.1190/INT-2016-0217.1.
Qian, J., Wang, X.J., Collett, T.S., et al., 2018. Downhole log evidence for the coexistence of structure II gas hydrate and free gas below the bottom simulating reflector in the South China Sea. Mar. Petrol. Geol. 98, 662–674. https://doi.org/10.1016/j.marpetgeo.2018.09.024.
Qin, X.W., Lu, J.A., Lu, H.L., et al., 2020. Coexistence of natural gas hydrate, free gas and water in the gas hydrate system in the Shenhu Area, South China Sea. China Geol. 3 (2), 210–220. https://doi.org/10.31035/cg2020038.
Rüger, A., 1997. P-wave reflection coefficients for transversely isotropic models with vertical and horizontal axis of symmetry. Geophysics 62 (3), 713–722. https://doi.org/10.1190/1.1444181.
Sahoo, S.K., Marín-Moreno, H., North, L.J., et al., 2018. Presence and consequences of coexisting methane gas with hydrate under two phase water-hydrate stability conditions. J. Geophys. Res. Solid Earth 123 (5), 3377–3390. https://doi.org/10.1029/2018JB015598.
Shipboard Scientific Party, 1996. Site 995. In: Tréhu, A.M., Bohrmann, G., Rack, F.R., et al. (Eds.), Proc. Ocean Drill. Prog. Initial Report, vol. 164.
Shipboard Scientific Party, 2003. Site 1250. In: Paul, C.K., Matsumoto, R., Wallae, P.J., et al. (Eds.), Proc. Ocean Drill. Prog. Initial Report, 204.
Singh, S.C., Minshull, T.A., Spence, G.D., 1993. Velocity structure of a gas hydrate reflector. Science 260 (5105), 204–207. https://doi.org/10.1126/science.260.5105.204.
Sloan, E.D., Koh, C.A., 2008. Clathrate Hydrates of Natural Gases, third ed. CRC Press, Taylor & Francis Group, New York. https://doi.org/10.1201/9781420008494.
Taladay, K.B., Moore, G.F., 2015. Concentrated gas hydrate deposits in the Kumano forearc basin, Nankai Trough, Japan. Fire in the Ice 15 (1), 1–4.
Tréhu, A.M., Bohrmann, G., Rack, F.R., et al., 2003. Leg 204 summary. Proc. Ocean Drill. Progr. Initial Rep. 204, 1–75.
Wei, J.G., Fang, Y.X., Lu, H.L., et al., 2018. Distribution and characteristics of natural gas hydrates in the Shenhu Sea Area, South China Sea. Mar. Petrol. Geol. 98, 622–628. https://doi.org/10.1016/j.marpetgeo.2018.07.028.
Westbrook, G.K., Carson, B., Musgrave, R.J., et al., 1994. 7. Site 892. Proc. Ocean Drill. Progr. Initial Rep. 146 (1), 301–378.
Whiticar, M.J., Hovland, M., Kastner, M., et al., 1995. 26. Organic geochemistry of gases, fluid, and hydrates at the Cascadia accretionary margin. Proc. Ocean Drill. Prog. 146 (1), 385–397.
Yang, S.X., Lei, Y., Liang, J.Q., et al., 2017. Concentrated gas hydrate in the Shenhu area, South China Sea: results from drilling expeditions GMGS3 & GMGS4. In: Proceedings of the 9th International Conference on Gas Hydrates (ICGH 2017). Denver, USA.
Ye, J.L., Qin, X.W., Xie, W.W., et al., 2020. The second natural gas hydrate production test in the South China Sea. China Geol. 3 (2), 197–209. https://doi.org/10.31035/cg2020043.
Zhan, L.S., Kang, D.J., Lu, H.L., et al., 2022. Characterization of coexistence of gas hydrate and free gas using sonic logging data in the Shenhu Area, South China Sea. J. Nat. Gas Sci. Eng. 101, 104540. https://doi.org/10.1016/j.jngse.2022.104540.
Zhu, L.Q., Sun, J., Zhou, X.Q., et al., 2023. Well logging evaluation of fine-grained hydrate-bearing sediment reservoirs: considering the effect of clay content. Pet. Sci. 20 (2), 879–892. https://doi.org/10.1016/j.petsci.2022.09.018.
Zhu, Y.J., Yang, X.M., Huang, X., et al., 2024. Acoustic characterization of hydrate formation and decomposition in clay-bearing sediments. Pet. Sci. 21 (4), 2830–2838. https://doi.org/10.1016/j.petsci.2024.06.008.